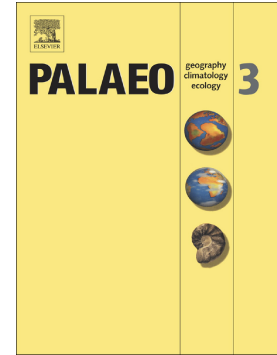


## Journal Pre-proof

Improving the detection of shell alteration: Implications for sclerochronology

Rute Coimbra, Stefan Huck, Niels J. de Winter, Ulrich Heimhofer, Philippe Claeys



PII: S0031-0182(20)30413-2

DOI: <https://doi.org/10.1016/j.palaeo.2020.109968>

Reference: PALAEO 109968

To appear in: *Palaeogeography, Palaeoclimatology, Palaeoecology*

Received date: 27 April 2020

Revised date: 27 July 2020

Accepted date: 27 July 2020

Please cite this article as: R. Coimbra, S. Huck, N.J. de Winter, et al., Improving the detection of shell alteration: Implications for sclerochronology, *Palaeogeography, Palaeoclimatology, Palaeoecology* (2020), <https://doi.org/10.1016/j.palaeo.2020.109968>

This is a PDF file of an article that has undergone enhancements after acceptance, such as the addition of a cover page and metadata, and formatting for readability, but it is not yet the definitive version of record. This version will undergo additional copyediting, typesetting and review before it is published in its final form, but we are providing this version to give early visibility of the article. Please note that, during the production process, errors may be discovered which could affect the content, and all legal disclaimers that apply to the journal pertain.

© 2020 Published by Elsevier.

## 1 **Improving the detection of shell alteration: implications for sclerochronology**

2  
3 Rute Coimbra<sup>a,\*</sup> [rcoimbra@ua.pt](mailto:rcoimbra@ua.pt); Stefan Huck<sup>b</sup> [huck@geowi.uni-hannover.de](mailto:huck@geowi.uni-hannover.de); Niels J. de Winter<sup>c,d</sup>  
4 [niels.de.winter@vub.be](mailto:niels.de.winter@vub.be); Ulrich Heimhofer<sup>b</sup> [heimhofer@geowi.uni-hannover.de](mailto:heimhofer@geowi.uni-hannover.de); Philippe Claeys<sup>c</sup>  
5 [phclaeys@vub.be](mailto:phclaeys@vub.be)

6 a) GeoBioTec, Departamento de Geociências, Universidade de Aveiro, Portugal

7 b) Institut of Geology, Leibniz University Hannover, Germany

8 c) Analytical, Environmental and Geochemistry Department, Vrije Universiteit Brussel, Pleinlaan 2, 1050 Brussels,  
9 Belgium

10 d) Department of Earth Sciences, Faculty of Geosciences, Utrecht University, the Netherlands

11 \*Corresponding author at: Rute Coimbra, Dpto. Geociências, Universidade de Aveiro, Campus de  
12 Santiago, 3810-193 Aveiro, Portugal

### 13 **Abstract**

14 Sclerochronology makes use of (fossil) shell-archives to establish records  
15 allowing for investigation of high-resolution environmental dynamics. Nevertheless,  
16 this potential can often not be fully exploited due to the interplay between  
17 paleoenvironmental variability, vital effects and the potential diagenetic modification of  
18 skeletal materials, which often results in highly complex records. A novel dynamic  
19 approach, aiming to separate pristine from altered shell material for paleoclimate and  
20 paleoenvironmental reconstructions is proposed.  
21

22 Seventeen fossil bivalve shells (requieniid rudists, pectinids and chondrodonts)  
23 from two neighbouring Lower Cretaceous (Albian) shallow-water sections (Lusitanian  
24 Basin, western Portugal) were analysed for their major and trace elemental  
25 compositions using high-resolution quantitative  $\mu$ XRF line scans. Their complex  
26 records were subject to a novel statistical analysis protocol, which tested mono- and  
27 multi-species datasets, as well as comparing shells from both locations.

28 Characteristic elemental associations reveal the differential impact of early and  
29 late diagenetic alteration processes. The incorporation of elements associated with  
30 detrital contribution (Fe, Si, Al) is attributed to syn-depositional bioerosion (shell-  
31 boring). In clear contrast, shell-portions showing a strong correlation between Fe and  
32 Mn are indicative of later diagenetic alteration. The influence of each process is

33 different at each site, revealing local differential alteration pathways. Mono-specific  
34 comparisons provides identical geochemical responses, suggesting that intra-specific  
35 differences do not control the observed elemental patterns. In contrast, inter-species  
36 tests rendered a clear separation in the way elements are incorporated in the shells of  
37 pectinids and requieniids (e.g., as evidenced by differences in Mg or Sr content). Such  
38 differences can be linked to differential biomineralization pathways, easily detected by  
39 the applied method.

40 We present a new, dynamic method for distinguishing pristine from altered shell  
41 material, not relying on arbitrary diagenetic thresholds for trace element content. By  
42 clearly identifying shell-alteration pathways, syn- to post-depositional processes are  
43 recognized. A progressive cleaning of the elemental dataset allows paleoenvironmental  
44 studies to be based on the most pristine data, contributing to unravelling the complex  
45 interplay between climate, environmental dynamics and their impact on  
46 biomineralization processes and sclerochronological archives.

47

48 Keywords: Shells, geochemistry, diagenesis, statistical analysis, paleoenvironment

49

## 50 **1- Introduction**

51 The study of past climate and environmental change yields crucial information  
52 about Earth's climate system and how global perturbations can affect the biosphere (e.g.  
53 Zachos et al., 2001). Most of these studies aim to characterize perturbations on a  
54 geological time scale (thousands to millions of years), identifying long term trends in  
55 climate, environment and ecology. Contrarily, the field of sclerochronology uses  
56 mineralogical, structural and chemical changes in accretionary biogenic archives to  
57 study changes in environment that take place on the scale of lifespans of the organisms  
58 (e.g. several years) that form these archives (e.g. Jones, 1983). These studies

59 complement longer timescale reconstructions and have the potential to yield snapshots  
60 of climate and environmental variability on a shorter timescale which can be placed in  
61 the context of longer timescale perturbations (e.g. Steuber et al., 2005). Bivalve shells  
62 have been an especially popular archive for sclerochronology work, because their  
63 growth rates are comparatively high (reported values up to 4 cm/yr; e.g. Batenburg et  
64 al., 2012; Schöne et al., 2005; Nedoncelle et al., 2013) and because the calcite shells of  
65 some species of bivalves (e.g. oysters and pectinids) are more resistant to diagenesis  
66 than their aragonitic counterparts (e.g. corals and gastropods, e.g. Brand and Veizer,  
67 1980; 1981).

68 In addition, growth lines and increments in the shells of fossil bivalves have  
69 been successfully applied to construct independent shell chronologies which allow  
70 researchers to accurately assess the timing and duration of shell formation and link shell  
71 chemistry to environmental variability in modern species (e.g. Richardson et al., 2004;  
72 Schöne et al., 2005; Gillikin et al., 2008). However, the complex interplay of multiple  
73 environmental, physiological and post-depositional (diagenetic) parameters on the  
74 chemical composition of bivalve shells has hampered the interpretation of the above-  
75 mentioned chemical variations in terms of environmental change. As a result,  
76 sclerochronologists often combine several chemical tracers in a multi-proxy approach in  
77 an attempt to disentangle the effects of different parameters on shell composition (e.g.  
78 Surge et al., 2001; de Winter et al., 2017a; 2018).

79 Elemental records obtained from biogenic calcite and/or aragonite have been  
80 used to reconstruct (paleo) environmental parameters (temperature, salinity, primary  
81 productivity, current patterns; e.g. Nürnberg et al., 1996; Halfar et al., 2000; Surge et  
82 al., 2001; Gillikin et al., 2008; Chan et al., 2011; Schöne et al., 2011; de Winter et al.,  
83 2017a; 2018; Ullmann et al., 2018; Huyghe et al., 2019; Markulin et al., 2019).



84 Nevertheless, strong differences in biomineralization pathway are often found to disrupt  
85 an already naturally complex signal, further hampered by the effects of diagenesis in  
86 fossil shell materials. The cautious use of statistical tools provides a valuable solution  
87 for this limitation.

88 Principal component analysis (PCA) is among the most popular multivariate  
89 statistical techniques for dealing with such large datasets, and is widely used across  
90 many scientific disciplines (Cordella, 2012; Yao et al., 2012; Coimbra et al., 2015,  
91 2018; Cai et al., 2019). PCA aims to extract, compress, simplify and analyse the  
92 structure of multivariate datasets. The inter-correlation of several dependent variables is  
93 tested and expressed as a set of new orthogonal variables (Principal Components- PC),  
94 evidencing the degree of similarity between observations and variables (Abdi and  
95 Williams, 2010 and references therein). In this study, as an innovative approach to  
96 sclerochronological data, a double PCA approach is applied (Coimbra et al., 2017), with  
97 a new automated adaptation (density analysis) for higher precision in isolating samples  
98 of interest.

99 The proposed data reduction approach simplifies the evaluation of elemental  
100 variations in shell archives highlighting taxon and habitat specific variations in trace  
101 element content. Environmental and diagenetic influence on original elemental  
102 composition can be addressed efficiently, allowing the identification of growth rhythms  
103 or responses of shell microstructure. This contribution provides significant advances in  
104 the detection of shell alteration, with the potential of refining sclerochronological  
105 interpretations for a variety of skeletal remains from a wide range of geological time  
106 periods.

107

108 **2- Geological and paleoenvironmental setting**

109 The well-exposed sections at São Julião (38.9319776°N, 9.4219073°W) and  
110 Praia das Maças (38.8297059°N, 9.468163°W) are located along the western coast of  
111 Portugal, within the southern sector of the Lusitanian Basin (Figs. 1 and 2). During the  
112 Cretaceous, the western Iberian plate was located at about 30°N (Stampfli and Borel,  
113 2002), under the influence of two major climatic zones: the mid-latitude warm humid  
114 belt and the northern hot arid belt (Chumakov et al., 1995). Throughout the Lusitanian  
115 Basin, a major unconformity marks the Aptian-Albian transition (Dinis and Trincão,  
116 1995; Heimhofer et al., 2007; Dinis et al., 2008). This regional unconformity is overlain  
117 by coarse-grained continental siliciclastics (Rozário Formation) deposited  
118 diachronously throughout the basin in fluvial-deltaic settings. These deposits are  
119 covered by nearshore strata and shallow-water platform carbonates of the Galé  
120 Formation. This formation is overlain by lagoonal and terrestrial deposits—the Caneças  
121 Formation.

122 The studied sedimentary succession comprises shallow-water carbonate-  
123 siliciclastic deposits (Figs. 2 and 3) assigned by previous workers to cover Albian to  
124 Early Cenomanian age (Rozário and Galé Formations; Hasenboehler, 1981; Medus,  
125 1982; Berthou, 1984; Rey, 1992; Horikx et al., 2014). The Albian Galé Formation is  
126 subdivided into the Água Doce and the Ponta da Galé Members (Rey, 1992). The  
127 lowermost Água Doce Member is mainly composed of alternating marly, carbonate-  
128 and sandstone-rich coastal-marine strata. More marine conditions are evidenced by  
129 increasingly thicker limestone beds towards the top of this member and mark the  
130 transition to the overlying carbonate-rich Ponta da Galé Member (Rey 1992). This work  
131 will focus on the stratigraphic interval covering the Ponta da Galé Member—the  
132 carbonate-rich upper portion of the Galé Formation, defined at the base by the regional  
133 occurrence of the first rudist beds, evidencing an overall deepening trend (Rey, 1992).

134 An overview of the main sedimentological, stratigraphical, and paleontological features  
135 of the São Julião and Praia das Maças sections is given in Fig. 3A. Based on previous  
136 work performed on these sections, the stratigraphic intervals under scope are well-  
137 known for not having experienced pervasive deep-diagenetic influence (Horikx et al.  
138 2014, 2016; Coimbra et al., 2017), justifying their use for exploring sclerochronological  
139 aspects. The regional stratigraphic correlation between both sections has been well-  
140 established using C-isotope stratigraphy, here partially reproduced after Horikx et al.  
141 (2014) (Fig. 3A). Accordingly, the base of the Praia das Maças section can be correlated  
142 to the second rudist-bearing bed at Sao Julião (165 m; Fig. 3A). Both sections are  
143 characterised by decreasing trend in C isotopes from bottom to top, despite minor  
144 differences in absolute value. Sampled shell materials retrieved from these deposits  
145 (examples in Fig. 3B) are investigated to explore the potential and evaluate the  
146 limitations of these shells as archives of paleoenvironmental change.

147

### 148 **3- Studied shell materials**

#### 149 3.1- *Pectinidae*

150 Nowadays, bivalves belonging to the superfamily Pectinidae (Rafinesque, 1815)  
151 (scallops) occupy a huge variety of habitats in polar, temperate and tropical seas,  
152 ranging from the intertidal zone to water depths up to 7000 m (Brand, 2006; Serb,  
153 2006). They can be byssally attached, free-living or encrusted and their life habit  
154 changes ontogenetically (Stanley, 1970). Largely, ancient pectinid shells such as those  
155 of *Amussiopecten baranensis* comprise an outer layer composed of (crossed, regular or  
156 irregular) foliated low-Mg calcite (LMC), a middle aragonitic layer and an inner  
157 foliated LMC layer (Zamarreño et al., 1996; Carter 1990). Commonly, shells of  
158 Cretaceous pectinids such as *Prohinnites favrinus* are predominantly composed of

159 foliated calcite (Harper et al., 1996). In fossil specimens, the inner crossed-lamellar  
160 aragonite layers are often replaced by coarse, sparry low-Mg calcite (Harper et al.,  
161 1996).

162

### 163 3.2- Rudists

164 Rudist bivalves (superfamily Hippuritoidea) are epibenthic sessile suspension-  
165 feeders that inhabited a variety of carbonate-dominated shallow water settings in the  
166 (sub-) tropical Tethyan-Atlantic-Pacific belt during late Mesozoic times (Gili et al.,  
167 1995; Skelton, 2003; Skelton, 2018; Gili and Götz, 2018). During the Cretaceous, they  
168 evolved to one of the most important neritic carbonate producers, with maximum  
169 carbonate production rates ranging between 2.2 and 35.7 kg per square meter per year  
170 (Steuber, 2000). In contrast to reef-building corals, rudists were typically loosely  
171 arranged in low-relief bioconstructions referred to as bouquets ( $n < 12$ ), clusters ( $n =$   
172  $> 12$ ) or thickets ( $n = > 100$ ; Philip, 1972; Gili et al., 1995). Significant differences in  
173 growth geometries (morphotypes) indicate that rudists were able to adapt to various  
174 habitats. Recumbent forms lay prone but unattached on mobile substrates in current-  
175 swept settings (Ross and Skelton, 1993). In contrast, the left valve of so-called  
176 ‘clingers’ was attached (cemented) to solid substrates (Skelton, 1978). During ontogeny,  
177 the elongated and initially cemented valve of predominantly cylindrical ‘elevators’  
178 stabilized by surrounding sediment or by neighbouring rudists (clustering; Gili and  
179 Götz, 2018).

180 In general, the shell of rudists comprises two layers: a rarely preserved inner  
181 layer originally composed of crossed lamellar aragonite and an outer low-Mg calcite  
182 layer composed of fibrous prisms (Skelton and Smith, 2000; Skelton, 2018). The  
183 mesostructural properties of the outer layer, however, show significant differences

184 among the rudist families (Skelton, 2018). Whereas Hippuritidae and Requiieniidae  
185 provide relatively compact and thick calcitic shells, the right valves of most Radiolitidae  
186 typically shows a complex celluloprismatic structure composed of numerous cells, often  
187 spar-filled after fossilization (Pons and Vicens, 2008).

188

#### 189 **4. Methods**

##### 190 4.1- Sample collection and preparation

191 Shells were cut to obtain thin sections and polished surfaces (Fig A1 for high-  
192 resolution images of all studied specimens). Selected shells were embedded in resin  
193 (Araldite® 2020, Huntsman, Basel, Switzerland) and subsequently cut along their major  
194 growth axis using a slow rotating rotary saw. A parallel slab was cut out of one-half of  
195 the shell, while the other half was preserved as archive half). For micro-XRF scanning,  
196 slabs were polished using silicon carbide polishing discs (up to P2400).

197

##### 198 4.2- Micro X-Ray Fluorescence

199 All polished shell surfaces were subject to non-destructive trace elemental  
200 analyses using micro-X-ray fluorescence (micro-XRF). Analyses were carried out with  
201 a Bruker M4 Tornado micro-XRF scanner (Bruker nano GmbH, Berlin, Germany) at  
202 the AMGC research group of the Vrije Universiteit Brussel (VUB, Brussels, Belgium).  
203 The Bruker M4 Tornado is equipped with a Rh metal-ceramic X-ray source operated at  
204 maximum energy settings (50 kV, 600  $\mu$ A). The X-ray beam was focused on a 25  $\mu$ m  
205 diameter circular spot (calibrated for Mo-K $\alpha$  radiation) and the intensity of returning X-  
206 rays was measured using two silicon drift detectors (see de Winter and Claeys, 2016).  
207 The sample position was controlled by a high-precision ( $\pm 1\mu$ m) XYZ sample stage that  
208 can be moved relative to the focused X-ray beam. Details on the setup and methodology

209 of the M4 Tornado XRF scanner can be found in de Winter and Claeys (2016) and de  
210 Winter et al. (2017a). Two types of analyses were carried out: semi-quantitative  
211 elemental mapping and quantitative point-by-point line scanning.

212 Elemental mapping was carried out by stitching together horizontal line scans  
213 that were produced by moving the sample through the focused X-ray beam in  
214 continuous motion, using short acquisition times per 25  $\mu\text{m}$  wide spot (20 ms). This  
215 acquisition time is insufficient for full quantitative analyses of individual points.  
216 Therefore, 2D-grids of relative trace element abundance were constructed by integrating  
217 the intensity under element X-ray fluorescence peaks and plotting differences in XRF  
218 intensity over the entire sample surface. These maps serve as a qualitative assessment of  
219 the nature of the material, guiding the position of quantitative XRF line scans (Fig. 4B  
220 to G). In this way, the exact path to follow during line scans was established ensuring  
221 minimal contribution of heavily altered shell portions (Fig. 4D and H).

222 Quantitative point-by-point micro-XRF line scans were carried out using longer  
223 integration times (60 s per point). Contrary to map analyses, line scans were carried out  
224 point by point rather than by means of continuous scanning. This approach allows the  
225 X-ray beam to stay on the same spot for enough time to reduce the signal to noise ratio  
226 of the XRF spectrum sufficiently for point-by-point quantification. The minimum time  
227 required for quantitative point analyses was determined by repeated analyses of  
228 carbonate reference materials following the protocol detailed in de Winter et al.  
229 (2017b). Spectra were quantified using the Bruker Esprit software calibrated using the  
230 matrix-matched BAS-CRM393 limestone standard (Bureau of Analyzed samples,  
231 Middlesbrough, UK), after which individual measurements were calibrated offline using  
232 seven matrix-matched international certified reference materials (CCH1, COQ1,  
233 CRM393, CRM512, CRM513, ECRM782, and SRM1d; see de Winter et al., 2018 for

234 details), which were treated as samples. Untreated trace element results are reported in  
235 Data\_Appendix. The applied set of standards collectively contained enough certified  
236 values to allow concentrations to be quantified (calibration line  $R^2 > 0.98$ ) for the  
237 elements Mg, Al, Si, K, Ca, Ti, Cr, Mn, Fe, Cu, Sr, Y and Ba. Other elements with less  
238 well constrained calibration lines ( $R^2$  values between 0.9 and 0.98) include P, Zn, Zr,  
239 Nb and Pb. These elements are more difficult to quantify because their XRF peaks tend  
240 to overlap with elements which are more common in bivalve carbonate (see de Winter  
241 and Claeys, 2016). These latter elements did not meet strict standards for quantification,  
242 but their semi-quantitative results can still be used to assess relative differences in  
243 elemental composition using the proposed double PCA and density analysis method.  
244 Details on reproducibility errors and detection limits are provided in the Appendix  
245 (Table A1).

246

#### 247 4.3- Statistical analysis: the double PCA+ approach

248 The double Principal Component Analysis was previously proven to be useful in  
249 shallow-marine contexts (Columba et al., 2017; details in Appendix). To determine the  
250 selection of elements to include in the analysis, an exploratory PCA is performed in  
251 order to detect the most significant (loadings  $< -0.5$  and  $> 0.5$ ) geochemical variables for  
252 each considered dataset (see Fig. A2 in Appendix). This ensures that the following  
253 double PCA method is carried out exclusively for the variables showing higher degree  
254 of affinity, using the statistical software package XLSAT, an add-in to Excel (detailed  
255 steps in Appendix). Here it is adapted to process the dense sclerochronological  
256 elemental datasets produced by micro-XRF in order to provide clues on the processes  
257 acting upon these mid-Cretaceous shells during their lifetime and after deposition. We  
258 expand the double PCA method by adding density analysis, performed using PAST

259 statistic package (Hammer et al., 2001, version 3.25)—an automated criterion for  
260 accurately delimiting different clusters of samples within a dataset (see Fig. A2 in  
261 Appendix for stepwise description and Figs. A3 and A4 in for further  
262 recommendations). Accordingly, data points included in the range of 2/3 of the  
263 maximum data density and within delimiting regular shaped contour lines are accepted  
264 as valid (Fig. A2C). This implies that data points plotting further away from the main  
265 cluster, which also generate distortion along the contour lines, are excluded from further  
266 computation. This improved version—double PCA+—can be applied to various  
267 combinations of datasets (one shell-transect, several transects, several sites, etc). The  
268 information generated by the double PCA+ is threefold: (i) it explores the array of  
269 possible mechanisms accounting for shell-alteration, (ii) provides arguments to isolate  
270 the best-preserved data, unlocking masked paleoenvironmental fluctuations; (iii)  
271 provides customized thresholds of shell-preservation, highlighting particularities of  
272 given sites or species. As the complete dataset comprises several geochemical variables  
273 extracted from seventeen shells belonging to two localities, the possibilities for  
274 comparison are large. The reasoning followed during this work was to select sets of  
275 specimens suitable to perform mono-specific and multi-species analysis for each  
276 location; followed by mono-specific analysis comparing both locations. Any other  
277 selection would be equally valid, depending on the aim of the study (e.g., targeting  
278 specific elements of interest; ancient specimens with better constrained ecological  
279 requirements; ancient versus modern examples; modern examples only).

280

## 281 **5- Results**

### 282 5.1- Conventional multi-proxy analysis



283 The large volume of information gathered during this research surpassed  
284 200.000 individual elemental values. The conventional approach of plotting the  
285 elemental data against shell length (example given in Fig. 5) can only be used when  
286 comparing a low number of transects amongst each other, otherwise plots become too  
287 large and confusing. For the pectinid shells from both locations, the obtained range of  
288 absolute values was different (Fig. 5). For example, baseline Mn values for the pectinid  
289 specimen from Praia das Maçãs are much higher than those obtained for the São Julião  
290 specimen, as well as the maximum peak values. This also holds true for all other  
291 presented elements (Fe, Sr and Mg). The temporal trends are hard to deduce due to  
292 frequent disruptions by sharp maximum peak values (noted in Fig. 5). Portions of shell  
293 with persistently high or low elemental values were also observed (e.g., high Sr values  
294 in Fig. 5). In order to compare the 17 specimens under scope, an alternative data-  
295 reduction method was required—the t-SNE PCA+ (see Appendix). Such a dense data  
296 cloud would distract from the differences between specimens, species and sites or  
297 concentration differences arising from differences in shell preservation.

298

## 299 5.2- Praia das Maçãs: mono-specific versus multi-species

300 For the locality of Praia das Maçãs, two groups of specimens were tested. The  
301 first group is mono-specific (Fig. 6A), with six (taxonomically undifferentiated)  
302 requiniid shells showing tightly clustered data, without evidence of major differences in  
303 elemental content. This clustering of samples forms a high-density area in the PCA-  
304 space (Fig. 6A), including 65% of the samples included in this group of shells. These  
305 were then used to establish the customized elemental threshold values of the most  
306 significant elemental proxies (see Fig. 6A and Appendix for detailed workflow). A  
307 rather large number of samples (35% of the total) fall out of this main cluster, largely

308 following a common trend towards higher Fe, Mn and Mg content (Fig. 6A, see also  
309 Fig. A5). In fact, these samples even seem to form a smaller cluster in the density plot.  
310 Only a very small group of samples does not follow this trend, plotting towards higher  
311 Si and S abundance (lowermost portion of the PCA space, Figs. 6A and A5).

312 The second set of samples from Praia das Maças is composed of 7 shells  
313 belonging to 4 different species (Chondrodont, hippuritid elevator rudist, pectinid and  
314 radiolitid; Figs. 6B and A4). A main data density area (see details on density analysis in  
315 Appendix) is defined by 85% of the samples of this group leading to a tight cluster  
316 despite the presence of different species. Only a minority of samples plot towards  
317 negative values of PC1, in response to higher concentration of Fe, Mn and Mg; and  
318 towards the more positive range of PC2 pointing at higher abundances of Si. When  
319 considering the sample distribution per specimen, the elevator rudist and pectinid shells  
320 are both slightly shifted towards higher Sr content. Additionally, the pectinid shell  
321 presents more samples responsible for the trend towards higher Si values.

322 When considering both sets of samples (mono- and multi-species), no major  
323 differences in elemental trends were observed (Figs. 6 and A5 in Appendix).  
324 Nevertheless, it is noteworthy that the mono-specific set denoted more variability in Fe,  
325 Mn and Mg (PC1 in Fig. 6A) as well as Si (PC2 in Fig. 6A); whilst the multi-species  
326 group revealed slight differences in Sr content, but overall good agreement in elemental  
327 abundance of the measured proxies (Fig. 6B).

328

### 329 5.3- São Julião: mono-specific versus multi-species

330 Specimens from the São Julião section were initially tested as a multi-species  
331 group including two *Apricardia carentonensis* shells and two pectinid shells (Figs. 7  
332 and A5 in Appendix). The double PCA+ provided two clearly differentiated clusters

333 defined by both species, largely attributable to significant differences in Sr and Pb  
334 content (Fig. 7A). In fact, by applying the density analysis criteria, the selected set of  
335 samples was largely composed of datapoints belonging to pectinid shells (ca. 78%),  
336 imposing an unwanted bias to this analysis. A mono-specific analysis was therefore  
337 preferred for these shells.

338 The dataset was consequently divided into two mono-specific sets: two  
339 *Apricardia* shells (Fig. 7B) and two pectinid shells (Fig. 7C). The *Apricardia* shells  
340 clustered tightly within a high-density area comprising ca. 80% of the samples. This set  
341 of samples was used to establish the elemental thresholds for this setting and species.  
342 Samples showing a clear trend towards lowered Ca abundance, along with higher Mg,  
343 Fe and Al content (PC1; Fig. 7B) fall out of the main cluster. Only a minor number of  
344 samples revealed the influence of trace Br and P concentration, showing an opposite  
345 trend (PC2; Fig. 7B). The two pectinid shells revealed a similar elemental profile when  
346 compared to *Apricardia* specimens: a main cluster generated by 65% of the samples,  
347 disrupted by samples denoting higher Mg, Fe, Si and S across PC1; and less significant  
348 incorporation of trace elements such as Pb, Br and Zn (Fig. 7C).

349

#### 350 5.4- São Julião versus Praia das Maças

351 Two pectinid shells retrieved at each of the studied sites were compared using  
352 the double PCA+ protocol (Figs. 8 and A5 as Appendix). Samples from both shells  
353 form a high-density cluster containing 80% of the total dataset, but samples from São  
354 Julião clearly dominate this accumulation (Fig. 8). This pattern is due to the higher  
355 variability in elemental composition evidenced by samples from the Praia das Maças,  
356 denoting a clear trend towards higher Mg, Fe, Mn and Br (PC1), along with lower Sr  
357 abundance (PC2). An alternative minor trend is also observed in pectinid data from

358 Praia das Maçãs, with a small set of samples responding to higher Si (and P) content  
359 (Fig. 8).

360

## 361 **6- Discussion**

362 In general, the PCA results are characterized by a high number of samples  
363 clustering tightly in all cases. As such, on average 75% of the total tested samples  
364 revealed a higher data density (see Fig. A2c in Appendix), forming a main cluster (Figs.  
365 6 to 8 and Fig. A5 as Appendix). In contrast, a small number of samples depart from  
366 this main cluster, forming different dispersion patterns (Figs. 6 to 8 and Table 1).  
367 Accordingly, the main cluster corresponds to the best-preserved samples, as evidenced  
368 by their low content in elements indicative of diagenetic alteration (e.g., Mn, Fe; Brand  
369 and Veizer, 1980; Al-Aasm and Veizer, 1986). Their high Sr content is also an  
370 indication of pristine shell material. This cluster contains information which can be  
371 interpreted in terms of paleoenvironmental conditions (Table 2). Contrarily, samples  
372 scattering away from the main cluster correspond to secondary processes (alteration)  
373 which occurred at any given state of the evolution of these biogenic materials. Persistent  
374 patterns of sample distribution were identified in the sets of tested shells (Figs. 6 to 8;  
375 summarized in Fig. 9). These patterns may respond to a wide array of variables,  
376 including biomineralization pathways, paleoenvironmental conditions and syn- to post-  
377 depositional alteration. Geochemical profiles can be interpreted in terms of species-  
378 dependence, site-specific processes and general disruption of the original signals; and  
379 the potential for isolating noise from paleoenvironmental information (Fig. 10). As an  
380 example of the benefits resulting from the Double PCA+ approach, Sr elemental values  
381 are addressed in Figure 11. The unprocessed raw elemental data obtained for the mono-  
382 specific set of six Requinid shells (see also Figs. 3 and A1) shows sharp variations,

383 largely towards very low abundance values (minimum value of 50 ppm; Fig. 11A). The  
384 dynamic elemental threshold values of 1204 to 1852 ppm obtained by the Double PCA+  
385 approach (Figs. 6 and 12; Table 1) provided a range of best-preserved datapoints,  
386 representing 80% of the unprocessed data. By applying this threshold, the resulting Sr  
387 plots for each shell now show a clearer variation patterns, denoting certain cyclicality in  
388 the sclerochronological record (Fig. 11B). The focus of this study is to improve the  
389 detection of shell alteration, hence the significance of short-term (seasonal/ontogenetic)  
390 elemental fluctuations enclosed in the “clean” sclerochronological record are beyond the  
391 scope of this contribution.

392 Focusing on the “clean” dataset generated by the application of the Double  
393 PCA+ method provided further validation, namely when dealing with mean elemental  
394 values of selected geochemical proxies (Mg and Sr; Table 2). Once shell alteration is  
395 detected and excluded from the dataset, the comparison between specimens, species and  
396 sites becomes straightforward. At São Julião, Mg concentrations are evidently higher  
397 for both Pectinid shells, when compared to *Apricardia* specimens. In fact, *Apricardia*  
398 shells at São Julião show the lowest Mg concentration of all tested shells (905 and 973  
399 ppm; Table 1). At Praia das Maças, Mg abundance is higher for Chondrodont specimens  
400 (3384 to 3823 ppm), also showing low Mg variability amongst them. This low intra-  
401 species Mg variability is also evident for requiniid specimens. Regarding Sr abundance,  
402 this element was not computed for some specimens from São Julião due to low  
403 statistical significance (Table 2 and Fig. 7). For the remaining shells, the obtained Sr  
404 record is rather stable, denoting lowered concentration only in the radiolithid shell (994  
405 ppm). For a better assessment of the good-preservation of the final dataset, Fe and Mn  
406 are also shown in Table 2, showing a narrow range of fluctuation in all shells and

407 absolute values of Fe from 56 to 342 ppm and Mn from 46 to 102 ppm (Mn was not  
408 computed for some specimens due to low statistical significance; Table 2).

409

#### 410 6.1- Main geochemical trends: processes and elemental responses

411 At Praia das Maças, both intra and inter-species datasets provided similar PCA  
412 patterns (Figs. 6 and 9A). Samples deviating towards the PCA region denoting higher  
413 Fe, Mn and Mg abundance (average values in Fig. 6) are interpreted as diagenetically  
414 compromised, recrystallized shell-portions (examples in Fig. 4A and E). Fe and Mn are  
415 typically enriched in calcite during diagenesis due to their solubility and high  
416 distribution coefficients (Veizer, 1983; Rimstidt et al., 1998; Swart, 2015).  
417 Accompanying the described Fe and Mn enrichment, Mg abundance also increases in  
418 these samples, with absolute values still within ILMC range (<4000 ppm; Fig. 6A). This  
419 reflects the loss of biogenic signature of the analysed calcite samples. Accordingly,  
420 originally lower Mg calcite portions of the shell (ca. 2500 ppm Mg; Fig. 6A and also  
421 chapter 3), also denote lower abundance in Sr (and Ca) due the recrystallization process  
422 (Brand and Veizer, 1980; A. Aasm and Veizer, 1982, 1986). These interpretations are  
423 based on the combined elemental features, which are more informative than reading  
424 isolated elemental values. The few samples deviating towards higher Si (and S) are  
425 interpreted as the result of the incorporation of siliciclastic material (pyrite not  
426 excluded) in borings by epifaunal organisms (Fig. 4A and B). The portions of the record  
427 remaining after the double PCA+ approach can then be interpreted in terms of  
428 environmental change. The double PCA+ therefore provides solid elemental threshold  
429 values (Fig. 6). When comparing intra and inter-species PCA results, most altered  
430 samples are contained in the sample set consisting of six requinid shells (Fig. 6A). This  
431 effect is due to the higher degree of similarity between the elemental records of each

432 shell within a mono-specific dataset, yielding higher-density data distribution along  
433 PCA plots (see section 4.3 and Fig. A2c for details on density analysis). This trend  
434 translates into narrower threshold values. In contrast, inter-species datasets generate  
435 lower density data distribution due to generation of more diffuse main clusters (example  
436 in Fig. 6B). For the latter, it also becomes evident that within the best-preserved data,  
437 certain species have higher Sr content (ca. 1500 versus 1200 ppm; Fig. 6B), as is the  
438 case of pectinid and radiolitid shells (Fig. 6B). This effect likely relates to a differential  
439 incorporation of Sr during shell growth and/or differences in shell microstructure (and  
440 microporosity), as all these specimens belong to the same site and geological time  
441 interval and were therefore subject to the similar diagenetic history (Fig. 3A). A  
442 species-dependent process may be envisaged, suggesting main differences in growth  
443 rate and/or calcification rate controlled Sr incorporation. The proposed calcification rate  
444 control on Sr operates in modern skeletal materials (Stoll and Schrag, 2000; Stoll et al.,  
445 2002; Rickaby et al., 2002; Carré et al., 2016), as well as in inorganic calcite (Lorenz,  
446 1981; Tesoriero and Pankow, 1990). Under higher calcification rates, Sr uptake occurs  
447 under kinetic control such that the animal cannot discriminate effectively against Sr,  
448 resulting in a higher distribution coefficient for this element— $D_{Sr}$  (Elderfield et al.,  
449 2002). The reported ontogenetic decrease in growth rates for rudists (Steuber, 1996) and  
450 oysters (Ullmann et al., 2010) supports the notion that shell-growth influences Sr  
451 incorporation.

452         At the São Julião section, inter-species differences were larger than in Praia das  
453 Maçãs, generating a clear separation between *Apricardia* and pectinid specimens (Fig.  
454 7A). It is noteworthy that pectinid shells, at this different location, also show a  
455 distinctive Sr signature (Fig. 7A). The most distinctive trait between *Apricardia* and  
456 pectinid shells is the concentration in Sr, which is on average 350 ppm higher in

457 *Apricardia* shells (1578 versus 1226 ppm). This feature supports the previous notion  
458 that ontogenic and/or metabolic control has a strong influence on Sr incorporation.  
459 When species are analysed separately, similar PCA patterns are found (Fig. 7B and C,  
460 see also Fig. 9B), with shell-alteration characterized by elevated concentration of the  
461 elemental association of Si, Fe, Al and Mg attributed to the influence of detrital  
462 siliciclastics included in bore holes (quartz and aluminosilicate minerals). Despite well-  
463 known difficulties related to the measurement of heavy metals with XRF, the minor  
464 incorporation of heavy metals (Pb, Zn) and Br is nevertheless relevant in both species  
465 (Fig. 7B, C), in part also related to an inverse trend of decreasing phosphorous  
466 abundance (Fig. 9B). Cautious comparison with modern examples may shed light into  
467 this trend. Bioaccumulation of naturally present trace elements is a well-known process  
468 in modern settings, of extreme relevance in the context of anthropogenic contamination  
469 on coastal areas and related mitigation efforts (Ferreira et al., 2004; Du et al., 2011;  
470 Markulin et al., 2019; VanPlantinga and Grossman, 2019). This process is of major  
471 concern regarding the soft tissue of bivalves (potentially for human consumption), but  
472 also affecting shell components. Primarily, the calcified layer of the shells is composed  
473 of a mineral phase, constituting over 95% of the shell mass. The remainder is the  
474 organic matrix (chitin, silk fibroin protein and acidic macromolecules) present as a thin  
475 envelope or sheet surrounding each mineral unit (Gregoire, 1972 in Heuer et al., 2002;  
476 Furuhashi et al., 2009). Intra-crystalline proteins occluded in the mineral lattice can also  
477 occur, potentially distorting the mineral lattice (Pokroy et al., 2006). This structure  
478 provides structural support, exerting control over the mineralization process (Jacob et  
479 al., 2009; Immenhauser et al., 2018). Proteins and carbohydrates have high affinity for  
480 heavy metals (Jacob et al., 2009), which can be remobilized during organic matrix  
481 degradation of ancient shells. Heavy metal and Br enrichment via the diagenetic



482 stabilization of organic components can potentially explain the presence of the  
483 persistent PCA trend observed on ancient shells of different species (Fig. 7B and C and  
484 Fig. 9B).

485 By combining data from the same species (pectinid shells) at different locations  
486 (Praia das Maças and São Julião), a combination of all the above processes becomes  
487 apparent (Fig. 8). The specimen from Praia das Maças shows clear evidence of more  
488 significant late diagenetic alteration, with more samples deviating towards the PCA  
489 space corresponding to higher Mn and Fe concentration. Significant shell-boring  
490 evidence (higher Al and Si values) is also detected at this location (Fig. 8). This result  
491 may hint at higher prevalence of syn-depositional bioerosion at Praia das Maças  
492 compared to São Julião and highlights the potential of the double PCA+ method for  
493 highlighting changes in paleoenvironment and –ecology. Conversely, the specimen  
494 collected at São Julião shows a tighter cluster along the PCA space, with only a few  
495 samples deviating from the main group of samples.

496 From all the tested shell combinations, three main patterns of sample distribution  
497 were identified on the PCA plots (Fig. 9C to E). When dealing with mono-species  
498 analysis, altered samples deviate from a main cluster, responding differently to a variety  
499 of processes (Fig. 9C). For analysis including different species, two possibilities arise:  
500 there are no evident elemental differences between species, forming one single main  
501 cluster and altered samples respond similarly (Fig. 9D); or inter-species elemental  
502 incorporation is significantly different, generating more than one main cluster from  
503 which altered samples deviate (Fig. 9E). In a next step, separate analysis (per species) is  
504 recommended (as described in Fig. 7).

505

506 6.2- Disruption of background signal

507 Raw elemental data corresponding to single shell transects (e.g., Fig. 5) typically  
508 present baseline values corresponding to environmentally relevant information, but  
509 often masked by noise. These interruptions of the background signal may relate to  
510 intervals of several consecutive samples showing moderately higher or lower values in  
511 respect to the baseline (Fig. 10A; trend1); or to sharp peaks generated by a small  
512 number of samples presenting higher/lower values regarding the baseline (Fig 10A;  
513 trend2). In the first case, recrystallized portions of the measured transects (e.g.,  
514 cemented veinlets; Fig. 4A and E) are often the cause for this effect and the double  
515 PCA+ approach is effective in separating syn to post-depositional processes from the  
516 primary elemental signals (Fig. 10B). In the case of conspicuous peaks, corresponding  
517 to the elemental signal of small fractures and/or borings (Fig. 4A) or even instrumental  
518 noise, the impact of such a small number of samples on the overall trend is minimal,  
519 easily corrected when smoothing the paleoenvironmental data obtained after the double  
520 PCA+ (Fig. 10C).

521

### 522 6.3- Dynamic thresholds: filtering-out altered elemental signals

523 Commonly, elemental cut-off values—ranges of values considered for well-  
524 preserved ancient materials—are obtained from previous cases discussed in the  
525 literature (e.g. Brand and Veizer, 1980, 1981; Al-Aasm and Veizer, 1986a; b), based on  
526 well-preserved specimens tested by a wide array of techniques (petrographic inspection,  
527 geochemistry and others) and contrasted with closely related modern specimens (when  
528 available). Valuable paleoclimatic interpretations have also been produced by more  
529 sophisticated thresholds for diagenesis (Jones et al., 2009; de Winter et al., 2017a;  
530 2018). For the present case of Cretaceous rudists, early contributions by Al-Aasm and  
531 Veizer (1986a; b) and Steuber (1996) form the backbone of sclerochronological

532 research on these materials. For a better detection of shell-alteration, the threshold  
533 values in this study (Fig. 12 and Table 1) were obtained by performing the double  
534 PCA+ approach and confidently excluding altered samples from paleoenvironmental  
535 considerations. Applying these dynamic thresholds resulted in an average of 75% of the  
536 initial datasets for each specimen being preserved (Figs. 6 to 8 and A5), a good  
537 indication of the careful selection of specimens and overall good preservation state.  
538 When compared to available literature for examples of similar (geological) age (Steuber  
539 et al., 1999; Steuber, 2000; Tibljaš et al., 2004; Damas-Molla et al., 2006; Higuera et  
540 al., 2007), no major differences were detected in terms of the elemental range of well-  
541 preserved shell-portions (Fig. 12 and Table 1). More interestingly, traditionally used  
542 cut-off values were improved by using the case-sensitive approach—the double PCA+.  
543 This was the case for the majority of frequently used elemental thresholds, in general  
544 narrower than literature values (Fig. 12 and Table 1).

545         Additionally, because these are dynamic thresholds, based on each specific case  
546 under scope, they can be applied to different sets of shells, adapting to other studies  
547 with specific aims (e.g., targeting a specific element on different shells, comparing  
548 intra-shell variations; ancient *versus* modern comparisons). This means that each time  
549 the Double PCA+ is applied, different thresholds can be derived, hence the designation  
550 of “dynamic” elemental thresholds. Also, they are applicable to other carbonate archives  
551 (belemnites, oysters, corals, and many others). The application of the double PCA+  
552 allows researchers to work with more unconventional elemental data (Si, Pb, Br, among  
553 others), shedding light into their paleoenvironmental significance. To our knowledge,  
554 this is the first attempt to use such a wide array of geochemical proxies, opening up the  
555 possibility for exploring their use as proxies in future studies.

556

557

558 **7- Conclusions**

559 Dense and complex elemental archives of seventeen bivalve shells belonging to  
560 two neighbouring Upper Albian shallow-water sections (western Portugal) were  
561 explored using a thorough statistical analysis protocol, comparing mono- and multi-  
562 species datasets, as well as shells from different locations.

563 Several inferences can be learned from applying the double PCA+ approach:

564 (i) Syn- to post-depositional processes can easily be identified based on the  
565 characteristic elemental associations revealed by PCA results. These include the  
566 influence of diagenesis (Fe, Mn and Mg); shell-boring filled by terrigenous materials  
567 (persistent coupling of Si, Al, Fe and Mg); bioaccumulation of heavy metals (Pb, Zn)  
568 and Br due to stabilization of organic shell components;

569 (ii) Different elemental patterns may arise, depending on the variability of the sampled  
570 materials. For mono-species groups, the tight clustering of less-altered samples provides  
571 a very clear decoupling of sample, responding to syn and post-depositional processes.  
572 This may also be the case for multi-species datasets, but if the original differences in  
573 elemental incorporation are significant, several main clusters arise, which should be  
574 analyzed separately to disentangle species-specific from depositional effects on trace  
575 element content;

576 (iii) Background elemental signals (calcification mechanism and/or environmental) are  
577 typically interrupted by two main types of disruption: one locally affecting only a minor  
578 portion of the shell, thus characterized by sharp and very significant changes in  
579 elemental composition (e.g., boring); the second affecting a larger portion of the shell,  
580 but in a less prominent elemental shift (e.g., recrystallizations);

581 (iv) Regardless the degree of shell-alteration, our PCA+ approach successfully isolated  
582 paleoenvironmental signals. The less-altered portions of the shells provided the  
583 establishment of dynamic cut-off values, customized for each set of shells and in overall  
584 agreement with elemental data retrieved from the literature. More unconventional  
585 elemental data also responded well to the double PCA+ approach, contributing with  
586 new clues for unravelling their incorporation mechanisms in ancient shells (Cu, P, S, Cl,  
587 K, Br, Zn, Pb).

588 This research provides new and relevant methodological advances, underlining  
589 the need to explore this and other tools that counterbalance the increasing technical  
590 ability to obtain dense, but highly intricate sclerochronological datasets and the most  
591 efficient way to unveil hidden, but relevant paleoenvironmental information. Expanding  
592 the use of the presented double PCA+ approach to other skeletal materials and time  
593 slices is thus a promising path towards a deeper understanding of past climatic  
594 dynamics, biomineralization processes and shell-archives and diagenetic pathways over  
595 time, promoting their use as proxies in future studies.

596

### 597 **Acknowledgements**

598 R. Coimbra is supported by Fundação para a Ciência e Tecnologia- FCT, Portugal and the  
599 research unit GeoBiotec - UIDB/04035/2020. Collection and preparation of fossil shell  
600 material was supported by DFG grant HE4467/6-1 to U. Heimhofer. PC thanks  
601 Research Foundation Flanders FWO-Hercules foundation for the acquisition of the  
602  $\mu$ XRF instrument, and VUB Strategic Research. NdW is a Flemish Research  
603 Foundation (FWO; 12ZB220N) post-doctoral fellow, and is supported by a MSCA  
604 Individual Fellowship (H2020-MSCA-IF-2018; 843011 – UNBIAS).

605

606 Conflict of Interest

607 All authors declare that no conflict of interest exists regarding the content on this  
608 contribution.

609

610 **References**

611 Abdi, H., Williams, L.J., 2010. Principal component analysis. Wiley Interdisciplinary  
612 Reviews: Computational Statistics 2, 433-459.

613 Al-Aasm, I.S. and Veizer, J.J., 1982. Chemical stabilization of low-magnesium calcite:  
614 an example of brachiopods. Journal of Sedimentary Petrology, 52, 1101-1109.

615 Al-Aasm, I.S., Veizer, J., 1986a. Diagenetic stabilization of aragonite and low-Mg  
616 calcite, II. Stable isotopes in rudists. Journal of Sedimentary Research 56, 763-770.

617 Al-Aasm, I.S., Veizer, J., 1986b. Diagenetic stabilization of aragonite and low-Mg  
618 calcite, I. Trace elements in rudists. Journal of Sedimentary Research 56, 138-152.

619 Batenburg, S.J., Reichert, G.-J., Jilbert, T., Jansen, M., Wesselingh, F.P., Renema, W.,  
620 2011. Interannual climate variability in the Miocene: High resolution trace element  
621 and stable isotope ratios in giant clams. Palaeogeography, Palaeoclimatology,  
622 Palaeoecology 306, 75-81.

623 Berthou, P.-Y., 1984. Albian-Turonian stage boundaries and subdivisions in the  
624 western Portuguese Basin, with special emphasis on the Cenomanian-Turonian  
625 boundary in the ammonite facies and rudist facies. Bulletin of the Geological  
626 Society of Denmark 33, 41-45.

627 Brand, R., 2006. Scallop ecology: distributions and behaviour. *In*: Shumway, S.E.,  
628 Parsons, G.J. (Eds.), *Scallops: Biology, Ecology and Aquaculture*. Elsevier B.V,  
629 Amsterdam, The Netherlands, 651-744.

630 Brand, U., Veizer, J., 1980. Chemical diagenesis of a multicomponent carbonate system  
631 - 1: Trace elements. Journal of Sedimentary Research 50, 1219-1236.

632 Brand, U., Veizer, J., 1981. Chemical diagenesis of a multicomponent carbonate  
633 system-2: stable isotopes. Journal of Sedimentary Research 51, 987-997.

- 634 Cai, T., Wu, H., Qin, J., Qiao, J., Yang, Y., Wu, Y., Qiao, D., Xu, H., Cao, Y., 2019. In  
635 vitro evaluation by PCA and AHP of potential antidiabetic properties of lactic acid  
636 bacteria isolated from traditional fermented food. *LWT* 115, 108455.
- 637 Carter, J.G., 1990. Skeletal biomineralization: patterns, processes and evolutionary  
638 trends. Van Nostrand & Reinhold, New York, 832 pp.
- 639 Chan, P., Halfar, J., Williams, B., Hetzinger, S., Steneck, R., Zack, T., Jacob, D.E.,  
640 2011. Freshening of the Alaska Coastal Current recorded by coralline algal Ba/Ca  
641 ratios. *Journal of Geophysical Research: Biogeosciences* 116 (G1).
- 642 Carré, M., Bentaleb, I., Bruguier, O., Ordinola, E., Bañares, N.T., Fontugne, M., 2006.  
643 Calcification rate influence on trace element concentrations in aragonitic bivalve  
644 shells: Evidences and mechanisms. *Geochimica et Cosmochimica Acta* 70, 4906-  
645 4920.
- 646 Christ, N., Immenhauser, A., Amour, F., Mutti, M., Tomás, S., Agar, S.M., Alway, R.,  
647 Kabiri, L., 2012. Characterization and interpretation of discontinuity surfaces in a  
648 Jurassic ramp setting (High Atlas, Morocco). *Sedimentology* 59, 249-290.
- 649 Chumakov, N.M., Zharkov, M.A., Herman, A.B., Doludenko, M.P., Kalandadze, N.N.,  
650 Lebedev, E.A., Ponomarenko, A.G., Rautian, A.S., 1995. Climate belts of the  
651 mid Cretaceous time. *Stratigraphy and Geological Correlations* 3, 241-260.
- 652 Coimbra, R., Azerêdo, A.C., Cabral, M.C., 2018. Cretaceous coastal lagoon facies:  
653 Geochemical insights into multi-stage diagenesis and palaeoclimatic signals.  
654 *Cretaceous Research* 85, 60-77.
- 655 Coimbra, R., Horikx, M., Huck, S., Heimhofer, U., Immenhauser, A., Rocha, F., Dinis,  
656 J., Duarte, L.V., 2017. Statistical evaluation of elemental concentrations in shallow-  
657 marine deposits (Cretaceous, Lusitanian Basin). *Marine and Petroleum Geology* 86,  
658 1029-1046.

- 659 Coimbra, R., Immenhauser, A., Olóriz, F., Rodríguez-Galiano, V., Chica-Olmo, M.,  
660 2015. New insights into geochemical behaviour in ancient marine carbonates (Upper  
661 Jurassic Ammonitico Rosso): Novel proxies for interpreting sea-level dynamics and  
662 palaeoceanography. *Sedimentology* 62, 266-302.
- 663 Cordella, C.B.Y., 2012. PCA: The Basic Building Block of Chemometrics. In: Krull, I.  
664 S. (director), *Analytical Chemistry*, pp. 1-44.
- 665 Damas-Mollá, L., Aranburu-Artano, A., García-Garmilla, F., 2006. Resistencia a la  
666 alteración diagenética de conchas de *Chondrodonta* sp. en las calizas rojas del  
667 Aptiense-Albiense Inferior de Ereño (Bizkaia). *Geogaceta*, 40, 195-198.
- 668 de Winter, N. J., & Claeys, P. (2016). Micro X-ray fluorescence ( $\mu$ XRF) line scanning  
669 on Cretaceous rudist bivalves: A new method for reproducible trace element profiles  
670 in bivalve calcite. *Sedimentology*, 64(1), 234-251.
- 671 de Winter, N. J., Goderis, S., Dehaire, F., Jagt, J. W., Fraaije, R. H., Van Malderen, S.  
672 J., et al. (2017a). Tropical seasonality in the late Campanian (late Cretaceous):  
673 Comparison between multiproxy records from three bivalve taxa from Oman.  
674 *Palaeogeography, Palaeoclimatology, Palaeoecology*, 485, 740-760.
- 675 de Winter, N. J., Sinnesael, M., Makarona, C., Vansteenberge, S., & Claeys, P. (2017b).  
676 Trace element analyses of carbonates using portable and micro-X-ray fluorescence:  
677 performance and optimization of measurement parameters and strategies. *Journal of*  
678 *Analytical Atomic Spectrometry*, 32(6), 1211-1223.
- 679 de Winter, N. J., Vellekoop, J., Vorsselmans, R., Golreihan, A., Soete, J., Petersen, S.  
680 V., et al. (2018). An assessment of latest Cretaceous *Pycnodonte vesicularis*  
681 (Lamarck, 1806) shells as records for palaeoseasonality: a multi-proxy investigation.  
682 *Climate of the Past*, 14(6), 725-749.



- 683 Dinis, J. L., Rey, J., De Graciansky, P. C., 2002. The Lusitanian Basin (Portugal) during  
684 the late Aptian- Albian: Sequential arrangement, proposal of correlations, evolution.  
685 *Comptes Rendus Geoscience* 334 (10), 757-764.
- 686 Dinis, J. L., Trincão, P., 1995. Recognition and stratigraphical significance of the  
687 Aptian unconformity in the Lusitanian Basin, Portugal. *Cretaceous Research* 16 (2-  
688 3), 171-186.
- 689 Dinis, J.L., Rey, J., Cunha, P.P., Callapez, P., Pena dos Reis, R., 2008. Stratigraphy and  
690 allogenic controls of the western Portugal Cretaceous: an updated synthesis.  
691 *Cretaceous Research* 29, 772-780.
- 692 Du, Y., Lian, F., Zhu, L., 2011. Biosorption of divalent Pb, Cd and Zn on aragonite and  
693 calcite mollusk shells. *Environmental Pollution* 153, 1763-1768.
- 694 Elderfield, H., M. Vautravers, and M. Cooper, 2002. The relationship between shell size  
695 and Mg/Ca, Sr/Ca,  $\delta^{18}\text{O}$ , and  $\delta^{13}\text{C}$  of species of planktonic foraminifera.  
696 *Geochemistry, Geophysics, Geosystems* 3(8), 1-13.
- 697 Ferreira, A.G., Machado, A.L.S., Zaldon, I.R., 2004. Temporal and spatial variation on  
698 heavy metal concentrations in the bivalve *Perna perna* (LINNAEUS, 1758) on the  
699 northern coast of Rio de Janeiro State, Brazil. *Brazilian Archives of Biology and*  
700 *Technology* 47, 519-527.
- 701 Furuhashi, T., Schwarzinger, C., Miksik, I., Smrz, M., Beran, A., 2009. Molluscan  
702 shell evolution with review of shell calcification hypothesis. *Comparative*  
703 *Biochemistry and Physiology Part B: Biochemistry and Molecular Biology* 154,  
704 351-371.
- 705 Gili, E., Götz, S., 2018. Part N, Volume 2, Chapter 26B: Paleoecology of rudists.  
706 *Treatise Online* 103: 1-29.

- 707 Gili, E., Masse, J.P., Skelton, P.W., 1995. Rudists as gregarious sediment-dwellers, not  
708 reef-builders, on Cretaceous carbonate platforms. *Palaeogeography,*  
709 *Palaeoclimatology, Palaeoecology* 118, 245-267.
- 710 Gillikin, D.P., Lorrain, A., Paulet, Y.-M., André, L., Dehairs, F., 2008. Synchronous  
711 barium peaks in high-resolution profiles of calcite and aragonite marine bivalve  
712 shells. *Geo-Marine Letters* 28, 351-358.
- 713 Gillikin, D.P., Lorrain, A., Paulet, Y.M., André, L., Dehairs, F., 2008. Synchronous  
714 barium peaks in high-resolution profiles of calcite and aragonite marine bivalve  
715 shells. *Geo- Marine Letters* 28 (5-6), 351-358.
- 716 Gillikin, D.P., Wanamaker, A.D., Andrus, C.F.T., 2019. Chemical sclerochronology.  
717 *Chemical Geology* 526, 1-6.
- 718 Grégoire, C., 1972. Structure of the molluscan shell. In: Florkin, M., Scheer, B.T. (Eds.)  
719 *Chemical Zoology*. Academic Press, New York, Vol. 7, pp. 45-102.
- 720 Halfar, J., Zack, T., Kronz, A., Zachos, J.C., 2000. Growth and high-resolution  
721 paleoenvironmental signals of rhodoliths (coralline red algae): a new biogenic  
722 archive. *Journal of Geophysical Research: Oceans* 105 (C9), 22107-22116.
- 723 Hammer, Ø., Harper, D.A.G., Ryan, P.D., 2001. PAST: Paleontological statistics  
724 software package for education and data analysis. *Palaeontologia Electronica* 4(1),  
725 9pp.
- 726 Harper et al., 1996. Early Cretaceous cementing pectinid bivalves. *Cretaceous Research*  
727 17, 135-150.
- 728 Hasenboehler, B., 1981. Étude paleobotanique et palynologie de l'Albien et du  
729 Cénomaniien du "Bassin Occidental Portugais" au sud de l'accident de Nazaré  
730 (Portugal). Université Pierre et Marie Curie, Paris, Thèse 3ème Cycle.  
731 Unpublished PhD thesis, 348 pp.

- 732 Heimhofer, U., Hochuli, P. A., Burla, S., Weissert, H., 2007. New records of Early  
733 Cretaceous angiosperm pollen from Portuguese coastal deposits: Implications for the  
734 timing of the early angiosperm radiation. *Review of Palaeobotany and Palynology*  
735 144(1), 39-76.
- 736 Heuer, A.H., Su, X., Kamat, S., Ballarini, R., Buschow, K.H.J., Cahn, R.W., Flemings,  
737 M.C., Ilschner, B., Kramer, E.J., Mahajan, S., Veyssiüre, P., 2001. Shell: Properties.  
738 In: Jürgen Buschow, K. H., Cahn, R.W., Flemings, M. C., Ilschner, B., Kramer, E.,  
739 Mahajan, S., Veyssiüre, P. (Eds.), *Encyclopedia of Materials: Science and*  
740 *Technology*. Elsevier, Oxford, pp. 8462-8469.
- 741 Higuera, I.R., Garmilla, F.G., Skelton, P.W., 2007. Synchronology and diagenesis of  
742 Late Cretaceous radiolitids (Bivalvia, Hippuritacea), Spain. In: Scott, R.W. (Ed.),  
743 Cretaceous rudists and carbonate platform environmental feedback. *SEPM Special*  
744 *Publication*, 87, pp. 115-139.
- 745 Horikx, M., Heimhofer, U., Dinis, J., Huck, S., 2014. Integrated stratigraphy of shallow  
746 marine Albian strata from the southern Lusitanian Basin of Portugal. *Newsletters on*  
747 *Stratigraphy* 47, 85-106.
- 748 Horikx, M., Hochuli, P.A., Feist-Burkhardt, S., Heimhofer, U., 2016. Albian  
749 angiosperm pollen from shallow marine strata in the Lusitanian Basin, Portugal.  
750 *Review of Palaeobotany and Palynology* 228, 67-92.
- 751 Huyghe, D., de Rafelis, M., Ropert, M., Mouchi, V., Emmanuel, L., Renard, M.,  
752 Lartaud, F., 2009. New insights into oyster high-resolution hinge growth patterns.  
753 *Marine Biology* 166, 48.
- 754 Immenhauser, A., Schöne, B.R., Hoffmann, R., Niedermayr, A., 2018. Mollusc and  
755 brachiopod skeletal hard parts: Intricate archives of their marine environment.  
756 *Sedimentology* 63, 1-59.

- 757 Jacob, D.E., Soldati, A.L., Wirth, R., Huth, J., Wehrmeister, U., Hofmeister, W., 2008.  
758 Nanostructure, composition and mechanisms of bivalve shell growth. *Geochimica et*  
759 *Cosmochimica Acta* 72, 5401-5415.
- 760 Jones, D.S., 1983. Sclerochronology: Reading the Record of the Molluscan Shell:  
761 Annual growth increments in the shells of bivalve molluscs record marine climatic  
762 changes and reveal surprising longevity. *American Scientist* 71, 384-391.
- 763 Jones, K., Bronson, S., Brink, P., Gordon, C., Mosher-Smith, K., Brown, M., Chaudhry,  
764 S., Rizzo, A., Sigismondi, R., Whitehurst, M., Lukaszewski, A., Kranz, D., Bland,  
765 K., Gordan, D., Lobel, J., Sullivan, J., Metzger, M., Shea, C., Harris, C.,  
766 Kambhampati, M., 2009. Bivalve Characterization Using Synchrotron Micro X-Ray  
767 Fluorescence. *Acta Physica Polonica A* 115.
- 768 Kullberg, J. C., Rocha, R. B., Soares, A. F., Rey, J., Terrinha, P., Azerêdo, A. C.,  
769 Callapez, P., Duarte, L. V., Kullberg, M. C., Martins, L., Miranda, J. R., Alves, C.,  
770 Mata, J., Madeira, J., Mateus, C., Moreira, M., Nogueira, C.R., 2013. A Bacia  
771 Lusitaniana: Estratigrafia, Paleogeografia e Tectónica. In *Geologia de Portugal* (eds.  
772 R. Dias, A. Araújo, P. Terrinha and J-C. Kullberg). Volume 2, Escolar Editora,  
773 Lisbon, Portugal, pp 125-347.
- 774 LNEG-LGM, 2010. *Carta Geológica de Portugal à escala 1:1000000*, edição de 2010.  
775 Laboratório Nacional de Energia e Geologia, Lisbon, Portugal.
- 776 Lorens, R. B., 1981. Sr, Cd, Mn, and Co distribution coefficients in calcite as a function  
777 of calcite precipitation rate. *Geochimica et Cosmochimica Acta*, 45, 553-561.
- 778 Markulin, K.i., Peharda, M., Mertz-Kraus, R., Schöne, B.R., Uvanovič, H., Kovač, Ž.,  
779 Janeković, I., 2019. Trace and minor element records in aragonitic bivalve shells as  
780 environmental proxies. *Chemical Geology* 507, 120-133.

- 781 Medus, J., 1982. Palynofloristic correlations of two Albian sections of Portugal.  
782 Cuadernos Geología Ibérica 8, 781-809.
- 783 Nedoncelle, K., Lartaud, F., de Rafelis, M., Boulila, S., Le Bris, N., 2013. A new  
784 method for high-resolution bivalve growth rate studies in hydrothermal  
785 environments. Marine Biology 160, 1427-1439.
- 786 Nürnberg, D., Bijma, J., Hemleben, C., 1996. Assessing the reliability of magnesium in  
787 foraminiferal calcite as a proxy for water mass temperatures. Geochimica et  
788 Cosmochimica Acta 60, 803-814.
- 789 Philip, J., 1972. Paléoécologie des formations à rudistes du Crétacé supérieur -  
790 l'exemple du sud-est de la France. Palaeogeography, Palaeoclimatology,  
791 Palaeoecology 12, 205-222.
- 792 Pokroy, B., Fitch, A., Zolotoyabko, E., 2006. The Microstructure of Biogenic Calcite: A  
793 View by High-Resolution Synchrotron Powder Diffraction. Advanced Materials  
794 18, 2363-2368.
- 795 Pons, J.-M., Vicens, E., 2008. The structure of the outer shell layer in radiolitid rudists,  
796 a morphoconstructional approach. Lethaia 41, 219-234.
- 797 Rauch, M., 2005. Geochemie von Rudistenschalen - Beiträge zur Meerwasserchemie  
798 (Sr/Ca, Mg/Ca,  $\delta^{13}C$ ) und Paläoklima der Kreide. PhD thesis, 198 pp., Ruhr-  
799 University Bochum, Bochum, Germany.
- 800 Rey, J., 1992. Les unités lithostratigraphiques du Crétacé inférieur de la région de  
801 Lisbonne. Comunicações dos Serviços Geológicos de Portugal 78, 103-124.
- 802 Richardson, C.A., Peharda, M., Kennedy, H., Kennedy, P., Onofri, V., 2004. Age,  
803 growth rate and season of recruitment of *Pinna nobilis* (L) in the Croatian Adriatic  
804 determined from Mg: Ca and Sr: Ca shell profiles. Journal of Experimental Marine  
805 Biology and Ecology 299, 1-16.

- 806 Rickaby, R. E. M. , Schrag, D. P. , Zondervan, I. and Riebesell, U. (2002): Growth-rate  
807 dependence of Sr incorporation during calcification of *Emiliana huxleyi*, *Global*  
808 *Biogeochemical Cycles*, 16 (1), 1-8.
- 809 Rimstidt, J.D., Balog, A., Webb, J., 1998. Distribution of trace elements between  
810 carbonate minerals and aqueous solutions. *Geochimica et Cosmochimica Acta* 62,  
811 1851-1863.
- 812 Ross, D.J., Skelton, P.W., 1993) Rudist formations of the Cretaceous: A  
813 palaeoecological, sedimentological and stratigraphical review. *Sedimentology*  
814 *Review* 1, 73-91.
- 815 Schöne, B. R., Zhang, Z., Radermacher, P., Thébaud, J., Jacob, D. E., Nunn, E. V., &  
816 Maurer, A.-F. (2011). Sr/Ca and Mg/Ca ratios of ontogenetically old, long-lived  
817 bivalve shells (*Arctica islandica*) and their function as paleotemperature proxies.  
818 *Palaeogeography, Palaeoclimatology, Palaeoecology*, 302(1-2), 52-64.
- 819 Schöne, B.R., Fiebig, J., Pfeiffer, M., Gleß, R., Hickson, J., Johnson, A.L., Dreyer, W.,  
820 Oschmann, W., 2005. Climate records from a bivalved Methuselah (*Arctica*  
821 *islandica*, Mollusca; Iceland). *Palaeogeography, Palaeoclimatology, Palaeoecology*  
822 228, 130-148.
- 823 Schöne, B.R., Houk, S.D., Castro, A.D.F., Fiebig, J., Oschmann, W., Kröncke, I.,  
824 Dreyer, W., Gosselck, F., 2005. Daily growth rates in shells of *Arctica islandica*:  
825 assessing sub-seasonal environmental controls on a long-lived bivalve mollusk.  
826 *Palaios* 20, 78-92.
- 827 Serb, J.M., 2006. Reconciling morphological and molecular approaches in developing a  
828 Phylogeny for the Pectinidae (Mollusca: Bivalvia). In: Shumway, S.E., Parsons,  
829 G.J. (Eds.), *Scallops: Biology, Ecology and Aquaculture*. Elsevier B.V,  
830 Amsterdam, The Netherlands, 1-29.

- 831 Skelton, P.W., 1978. The evolution of functional design in rudists (Hippuritacea) and its  
832 taxonomic implications. Royal Society of London, Philosophical Transactions  
833 284, 305-318.
- 834 Skelton, P.W., 2003. The Cretaceous World. The Open University and Cambridge  
835 University Press. Cambridge, UK. 360 pp.
- 836 Skelton, P.W., 2018. Part N, Volume 1, Chapter 26A: Introduction to the Hippuritida  
837 (rudists): Shell structure, anatomy, and evolution. Treatise Online 104: 1-37.
- 838 Skelton, P.W., Smith, A.B., 2000. A preliminary phylogeny for rudist bivalves: Sifting  
839 clades from grades. In: Harper, E.M, Taylor, J.D., Crame, J.A. (Eds.): The  
840 Evolutionary Biology of the Bivalvia. Geological Society, London, Special  
841 Publications 177, 97-127.
- 842 Stampfli, G.M., Borel, G.D., 2002. A plate tectonic model for the Paleozoic and  
843 Mesozoic constrained by dynamic plate boundaries and restored synthetic oceanic  
844 isochrons. Earth and Planetary Science Letters 196, 17-33.
- 845 Stanley, S.M., 1970. Relation of shell form to life habits of the Bivalvia (Mollusca).  
846 Geological Society of America Memoires 125, 1-296.
- 847 Steuber, T., 1996. Stable isotope sclerochronology of rudist bivalves: Growth rates and  
848 Late Cretaceous seasonality. Geology, 24, 315-318.
- 849 Steuber, T., 1999. Isotopic and chemical intra-shell variations in low-Mg calcite of  
850 rudist bivalves (Mollusca-Hippuritacea): disequilibrium fractionations and late  
851 Cretaceous seasonality. International Journal of Earth Sciences 88, 551-570.
- 852 Steuber, T., 2000. Skeletal growth rates of Upper Cretaceous rudist bivalves:  
853 implications for carbonate production and organism-environment feedbacks. In:  
854 INSALCO, E. et al. (eds.): Carbonate Platform Systems: Components and  
855 Interactions. Geol. Soc. London, Spec. Publ., 178, 21-32.

- 856 Steuber, T., Rauch, M., Masse, J.-P., Graaf, J., Malkoč, M., 2005. Low-latitude  
857 seasonality of Cretaceous temperatures in warm and cold episodes. *Nature* 437,  
858 1341-1344.
- 859 Stoll, H.M., Klaas, C.M., Probert, I., Ruiz Encinar, J., Garcia Alonso, J.I., 2002.  
860 Calcification rate and temperature effects on Sr partitioning in coccoliths of multiple  
861 species of coccolithophorids in culture. *Global and Planetary Change* 34, 153-171.
- 862 Stoll, H.M., Schrag, D.P., 2000. Coccolith Sr/Ca as a new indicator of coccolithophorid  
863 calcification and growth rate. *Geochemistry, Geophysics, Geosystems* (1), 1006.
- 864 Surge, D., Lohmann, K. C., & Dettman, D. L. (2001). Controls on isotopic chemistry of  
865 the American oyster, *Crassostrea virginica*: implications for growth patterns.  
866 *Palaeogeography, Palaeoclimatology, Palaeoecology*, 172(3), 283-296.
- 867 Swart, P.K., 2015. The geochemistry of carbonate diagenesis: the past, present and  
868 future. *Sedimentology* 62, 123-134.
- 869 Tesoriero, A. J., and J. F. Pankow, 1996. Solid solution partitioning of  $\text{Sr}^{2+}$ ,  $\text{Ba}^{2+}$  and  
870  $\text{Cd}^{2+}$  to calcite. *Geochimica et Cosmochimica Acta*, 60, 1053-1063, 1.
- 871 Tibljaš, D., Moro, A., Ostrž, Z., 2004. Mineral and Chemical Composition of Rudist  
872 Valves from Upper Cretaceous Limestones of Southern Istria, Croatia. *Geologia*  
873 *Croatica*, 57 (1), 13-19.
- 874 Ullmann, C.V., Gale, A.S., Huggett, J., Wray, D., Frei, R., Korte, C., Broom-Fendley,  
875 S., Littler, K., Hesselbo, S.P., 2018. The geochemistry of modern calcareous barnacle  
876 shells and applications for palaeoenvironmental studies. *Geochimica et*  
877 *Cosmochimica Acta* 243, 149-168.
- 878 Ullmann, C.V., Wiechert, U., Korte, C., 2010. Oxygen isotope fluctuations in a modern  
879 North Sea oyster (*Crassostrea gigas*) compared with annual variations in seawater



880 temperature: Implications for palaeoclimate studies. *Chemical Geology* 277, 160-  
881 166.

882 VanPlantinga, A.A., Grossman, E.L., 2019. Trace elements in mussel shells from the  
883 Brazos River, Texas: environmental and biological control. *Biogeosciences*  
884 Discussions 2019, 1-27.

885 Veizer, J., 1983. Chemical analysis of carbonates: theory and application of trace  
886 element technique. In: Arthur, M.A., Anderson, T.F., Kaplan, I.R., Veizer, J. (Eds.),  
887 *Stable Isotopes in Sedimentary Geology*. SEPM Short Course No.10, pp. 1-100.

888 Yao, F., Coquery, J., Lê-Cao, K.-A., 2012. Independent Principal Component Analysis  
889 for biologically meaningful dimension reduction of large biological data sets. *BMC*  
890 *bioinformatics* 13, 24-24.

891 Zachos, J., Pagani, M., Sloan, L., Thomas, E., Ballups, K., 2001. Trends, rhythms, and  
892 aberrations in global climate 65 Ma to present. *Science* 292, 686-693.

893 Zamarreño et al., 1996. The shell microstructure, mineralogy and isotopic composition  
894 of *Amussiopecten bararensis* (Pectinidae, Bivalvia) from the Miocene of Spain:  
895 A valuable paleoenvironmental tool *Geobios* 29, 707-724.

896  
897 **Fig. 1.** Geographical setting of the studied locations. A) Map of Iberia showing the  
898 location of the western Portuguese coast. B) Regional distribution of Cretaceous  
899 outcrops (adapted from LNEG-LGM, 2010), along with delimitation of the Lusitanian  
900 Basin (after Kullberg et al., 2013). C) Location of study sites at São Julião and Praia das  
901 Maçãs (indicated by stars), south of Ericeira (Portugal).

902

903 **Fig. 2.** Field photographs and particular aspects of sampled beds and shells. A and B)  
904 Aerial photographs of Praia das Maçãs and near São Julião (extracted from  
905 <http://portugalfotografiaaerea.blogspot.com/>); C) Field aspect of one specific sampled

906 bed; D) Field aspect of the pectinid bearing bed at Praia das Maças (PM4); E) Field  
907 aspect of a requiniid-rich horizon at Praia das Maças (PM12); F) Detail of an  
908 *Apricardia carentonensis* shell from the São Julião section.

909

910 **Fig. 3.** Stratigraphic context, selected specimens and comparison scheme. A) Synthetic  
911 lithological log of São Julião and Praia das Maças showing height (in meters),  
912 stratigraphy, C-isotope values as complementary lateral correlation tool and the main  
913 sedimentological features (see Horikx et al., 2014 and Coimbra et al., 2017 for more  
914 detailed explanations). B) List of selected specimens and a scheme illustrating the logic of  
915 comparison followed during this work (see text for further details and Fig. A1 in  
916 Appendix for photographs of all used specimens). Numeral tags (in blue) link each shell  
917 (or group of shells) specimen to their stratigraphic position, used throughout this  
918 contribution.

919

920 **Fig. 4.** Shell structure and preliminary assessment of shell-preservation state. A to D)  
921 Example from Praia das Maças, including microscope detail of small borings and small  
922 cemented (sub-vertical) veinlet and elemental mapping of Mn and Sr, as well as the  
923 chosen transect for further geochemical line scanning. E to H) example from São Julião,  
924 with microscope detail of small borings and fractures affecting the shell and elemental  
925 mapping of Fe and Mn, as well as the selected transect for further line scanning (red  
926 line). Shell length ca. 8 cm in both cases, numeral tags (in blue) are according to Figure  
927 3 and Fig. A1 as Appendix).

928

929 **Fig. 5.** Selected raw elemental data (Mn, Fe, Sr, Mg) for two pectinid specimens  
930 collected at different locations (Praia das Maças and São Julião) illustrating the need of

931 an efficient data treatment approach. Note the high complexity of each elemental record,  
932 differences in absolute value and fluctuations along shell-length, as well as the  
933 difficulties on comparing the records of both shells. Numeral tags (in blue) are  
934 according to Figure 3 and Fig. A1 as Appendix.

935

936 **Fig. 6.** Principal component analysis results (scores and loadings), combined with  
937 density analysis (see Appendix for further details) for the specimens collected at Praia  
938 das Maças. Sample distribution by shell is also represented by using coloured dots,  
939 corresponding to the contribution of each shell to the cloud of data generated by the  
940 PCA procedure (in white dots). This representation is proportional to the main PCA  
941 plot, respecting the position of each sample along the PCA space. A) mono-specific  
942 analysis including six requiniid shells; B) multi-species analysis including seven  
943 different shells belonging to four species. Note tight clustering of a significant  
944 percentage of the samples delimiting a range of elemental thresholds, as well as similar  
945 elemental trend of deviation from the main cluster (see text for detailed explanation).  
946 Numeral tags (in blue) are according to Figure 3 and Fig. A1 as Appendix.

947

948 **Fig. 7.** Principal component analysis results (PCA scores and loadings), combined with  
949 density analysis (double PCA+; see Appendix for further details) for the specimens  
950 collected at São Julião. Sample distribution by shell is also represented by using  
951 coloured dots, corresponding to the contribution of each shell to the cloud of data  
952 generated by the PCA procedure (in white dots). This representation is proportional to  
953 the main PCA plot, respecting the position of each sample along the PCA space. A)  
954 multi-species analysis including four different shells belonging to two species; B and C)  
955 mono-specific analysis of samples included in A), separated by species (*Apricardia* and

956 pectinid, respectively). Note persistent elemental trends when considering different  
957 species (see text for detailed explanation). Numeral tags (in blue) are according to  
958 Figure 3 and Fig. A1 as Appendix.

959

960 **Fig. 8.** Principal component analysis results (PCA scores and loadings), combined with  
961 density analysis (double PCA+; see Appendix for further details) for pectinid shells  
962 collected at São Julião and Praia das Maças (mono-specific analysis). Sample  
963 distribution by shell is also represented. Note a tighter clustering of samples belonging  
964 to the pectinid shell collected at São Julião (see text for further explanations). Numeral  
965 tags (in blue) are according to Figure 3 and Fig. A1 as Appendix.

966

967 **Fig. 9.** Representative scheme of main elemental trends as depicted by double PCA+  
968 approach (see also Fig. A4). A and E) Summary of the persistent elemental trends and  
969 associations identified along the tested shells, with their respective process (diagenesis,  
970 boring, a combined effect of both and bioaccumulation); C to E) Example of sample  
971 distribution across the PCA space in response to the identified processes. Sample  
972 distribution will depend on which processes are involved (single or multiple) and on the  
973 variability of the biogenic record (mono vs. multi-species analysis).

974

975 **Fig. 10.** Schematic workflow for improving the detection of shell-alteration. A) Possible  
976 disruptions of background signal by significantly altered portions and/or cracks; B) fast  
977 detection of altered samples allows their elimination from further analysis, in order to  
978 obtain a cleaner and relevant paleoenvironmental signal; C) Isolating the clean  
979 background record allows the identification of intra-shell fluctuations, attributable to

980 seasonal climate in ancient times. Numeral tags (in blue) are according to Figure 3 and  
981 Fig. A1 as Appendix.

982

983 **Fig. 11.** Comparison between unprocessed elemental data and the resulting information  
984 after the Double PCA+ approach. A) Sr values for the set of 6 requiniid shells (tag  
985 numeral as in Figs. 3 and A1). White shaded area delimits the range of best-preserved  
986 Sr values, when Double PCA+ is computed for this specific group of shells (see statistic  
987 results in Fig. 6). B) Best-preserved Sr values for all requiniid shells, after excluding  
988 20% of the altered data by the Double PCA+ method (see text for details). The clean  
989 dataset of each shell now delineates discernible cyclic variations in Sr abundance. Note  
990 that the obtained elemental threshold values are customized for this set of mono-specific  
991 shells (see Fig. 12 and Table 1 for obtained values of other sets of shells).

992

993 **Fig. 12.** Dynamic elemental threshold values obtained by the application of the double  
994 PCA+ screening method (see Appendix for details) and data retrieved from available  
995 literature. Note overall agreement with published cut-off elemental values, as well and  
996 the establishment of new threshold for more unconventional elements (Cu, Zn, Pb, Cu).  
997 Numeral tags (in blue) are according to Figure 3 and Fig. A1 as Appendix.

998

999 **Table 1.** Dynamic elemental threshold values obtained by the application of the double  
1000 PCA+ screening method (see Appendix for details) and threshold values extracted from  
1001 literature. Groups 1 to 6 refer to used literature and tested shell combinations (same as  
1002 in Figure 11). Min=minimum; max=maximum. Numeral tags (in blue) are according to  
1003 Figure 3 and Fig. A1 as Appendix.

1004

1005 **Table 2.** Average elemental values (in ppm) resulting from the application of the double  
 1006 PCA+ approach (see Appendix for details). Shell tags as in Fig. 3 and A1.

1007  
 1008 Table 1- Dynamic elemental threshold values obtained by the application of the double PCA+ screening  
 1009 method (see Appendix for details) and threshold elemental values extracted from literature. Groups of  
 1010 shells 1 to 6 refer to used literature and tested shell combinations (same as in Figure 11; min=minimum;  
 1011 max=maximum).

	<b>Ca</b> (min; max)	<b>Mg</b> (min; max)	<b>Sr</b> (min; max)	<b>Fe</b> (min; max)	<b>Mn</b> (min; max)	<b>Al</b> (min; max)	<b>Si</b> (min; max)	<b>Cu</b> (min; max)	<b>S</b> (min; max)	<b>P</b> (min; max)	<b>Br</b> (min; max)	<b>Zn</b> (min; max)	<b>Pb</b> (min; max)
<b>1</b>	a)	1200; 4600	700; 7230	0; 420	0; 410	a)	a)	0; 24	a,	a)	a)	0; 20	0; 10
<b>2</b>	387666; 395206	359; 4911	888; 2000	0; 689	0; 170	--	1573; 6209	0; 50	--	--	--	--	--
<b>3</b>	392627; 397951	631; 3080	1204; 1852	0; 459	0; 266	--	821; 1985	--	71; 987	--	--	--	--
<b>4</b>	390535; 396651	568; 2892	986; 1734	0; 578	0; 130	138; 290	341; 5085	--	--	3; 27	0; 39	--	--
<b>5A</b>	392024; 395914	498; 1492	--	0; 310	--	225; 501	--	--	--	15; 29	10; 88	--	--
<b>5B</b>	393869; 395633	1031; 1821	--	0; 255	--	--	1783; 3223	--	307; 838	--	9; 20	15; 42	4; 30
<b>6</b>	a)	277; 1337	879; 1428	0; 46	0; 25	a)	a)	a)	a)	a)	a)	a)	a)

(a) Not found, presented, measured and/or assumed as constant value; -- Not computed due to low statistical significance (see text)

Group 1- literature\*; Group 2- Different species; same location (Praia das Maças) 5 6 7 8; Group 3- Same species; same location (Praia das Maças) 9  
 Group 4- Same species; different location (pectinid shells) 1 5; Group 5A- Same species, same location (Apricardia, São Julião) 3 4  
 Group 5B- Same species, same location (pectinid shells, São Julião) 1 2; Group 6- Different species; different locations (ICP-powder samples)

1012  
 1013  
 1014 **Table 2.** Average elemental values (in ppm) resulting from the application of the double PCA+ method  
 1015 (see Appendix for details). Shell tags as in Figs. 3 and A1.

<b>Location</b>	<b>Shell Tag</b>	<b>Mg</b>	<b>Sr</b>	<b>Fe</b>	<b>Mn</b>
<b>São Julião</b> section	Tag 1_pectinid 1	1597 <sup>(2)</sup>	1284 <sup>(2)</sup>	141 <sup>(2)</sup>	50 <sup>(2)</sup>
		1366 <sup>(3)</sup>	--	82 <sup>(3)</sup>	--
	Tag 2_pectinid 2	1465	--	111	--

	Tag 3_ <i>Apricardia</i> 1	905	--	56	--
	Tag 4_ <i>Apricardia</i> 2	973	--	58	--
	Tag 5_pectinidA	2212 <sup>(1)</sup> 2222 <sup>(2)</sup>	1512 <sup>(1)</sup> 1501 <sup>(2)</sup>	159 <sup>(1)</sup> 147 <sup>(2)</sup>	88 <sup>(1)</sup> 59 <sup>(2)</sup>
	Tag 6_Chondrodont 1	3668	1285	342	99
	Tag 6_Chondrodont 2	3823	1460	269	70
	Tag 6_Chondrodont 3	3384	1363	134	52
	Tag 6_Chondrodont 4	3795	1397	120	61
	Tag 7_elevator rudist	1174	1474	85	68
	Tag 8_radiolithid	3810	994	279	102
Praia das Maçãs section	Tag 9_Requiniid 1	1786	1640	58	83
	Tag 9_Requiniid 2	1801	1543	85	47
	Tag 9_Requiniid 3	1554	1465	92	51
	Tag 9_Requiniid 4	2283	1540	70	46
	Tag 9_Requiniid 5	1784	1530	111	46
	Tag 9_Requiniid 6	1805	1453	83	53

(1) computed in Group 2, see Figs. 6B and 12; (2) computed in Group 4, see Figs. 8 and 12; (3) computed in Group 5B, see Figs. 7C and 12; -- Not computed due to low statistical significance (see text)

1016

1017 Highlights

- 1018 • A novel dynamic method aims to separate pristine from altered shell material;
- 1019 • Syn- to post-depositional processes were easily identified;
- 1020 • PCA+ approach successfully isolated paleoenvironmental signals;
- 1021 • Different elemental patterns arise from mono- or multi-species sets of shells;
- 1022 • Dynamic elemental cut-off values are customized for each set of shells.

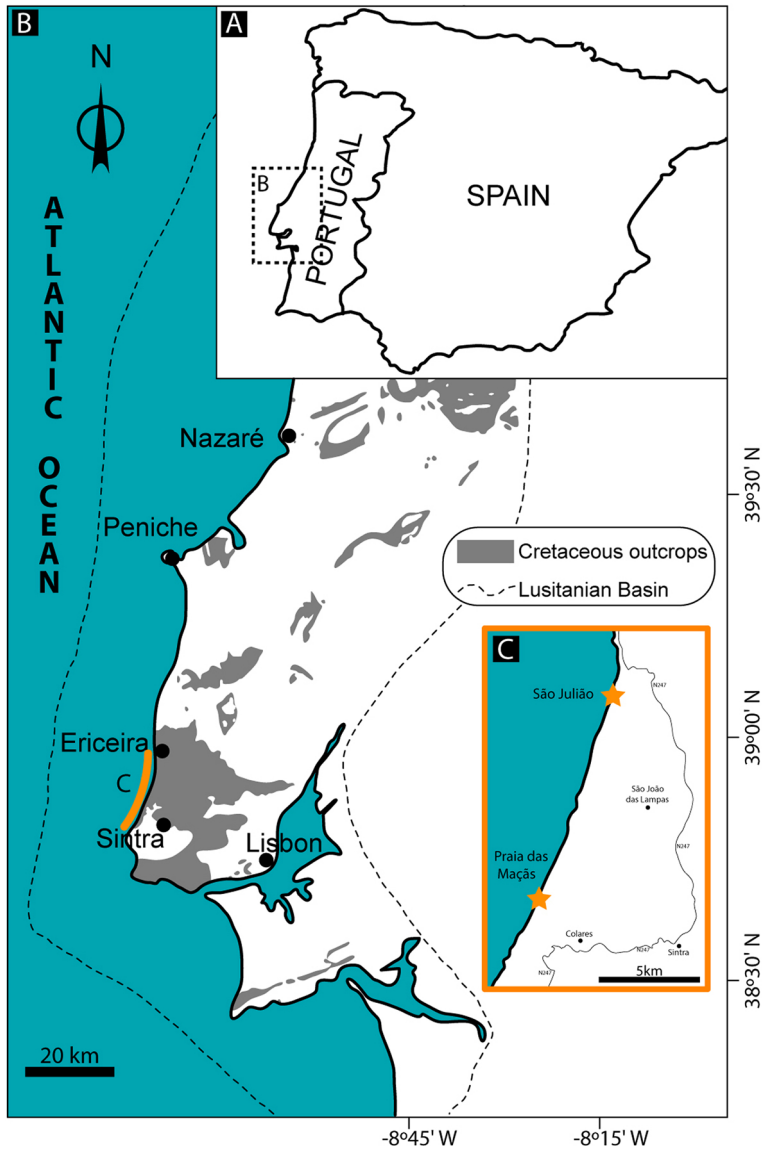


Figure 1





Figure 2

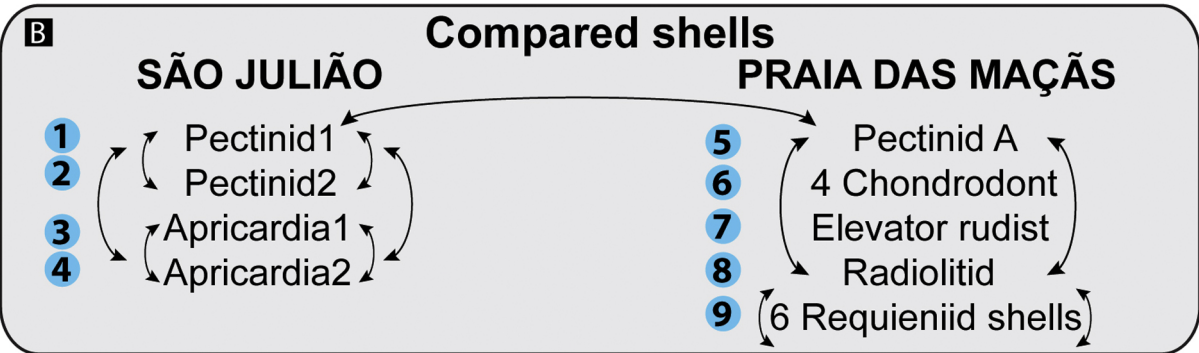
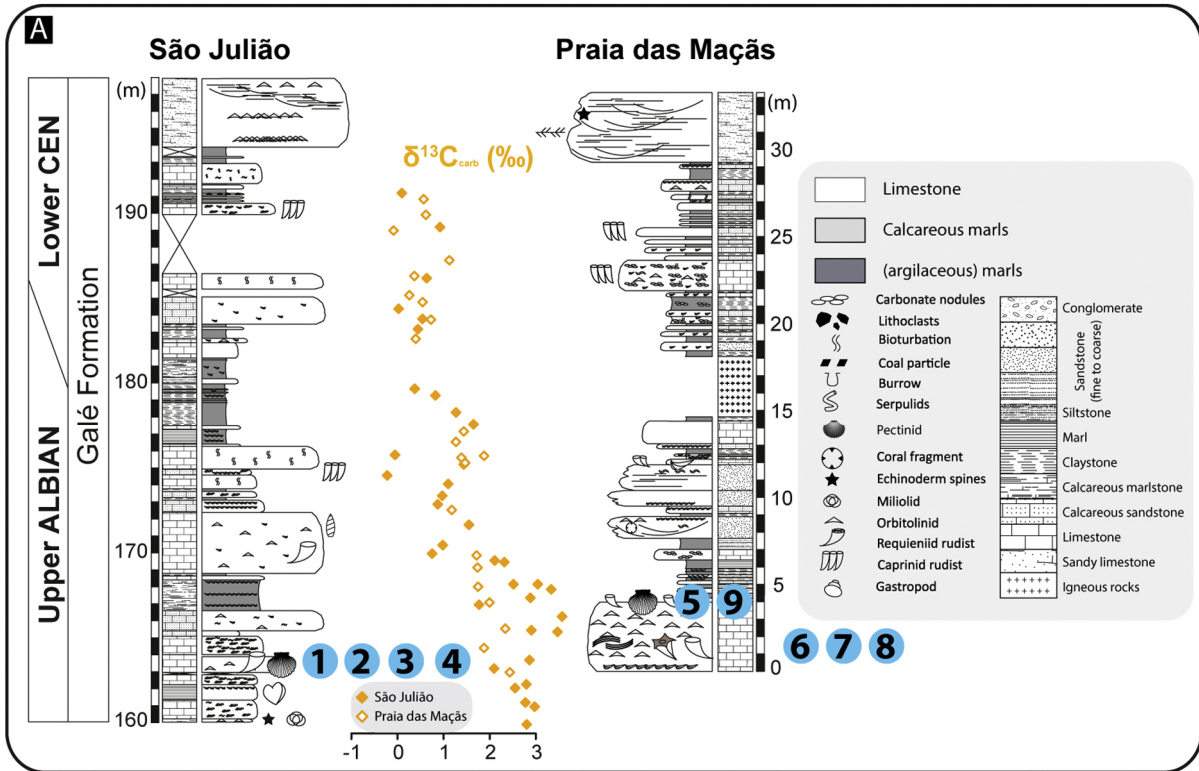


Figure 3



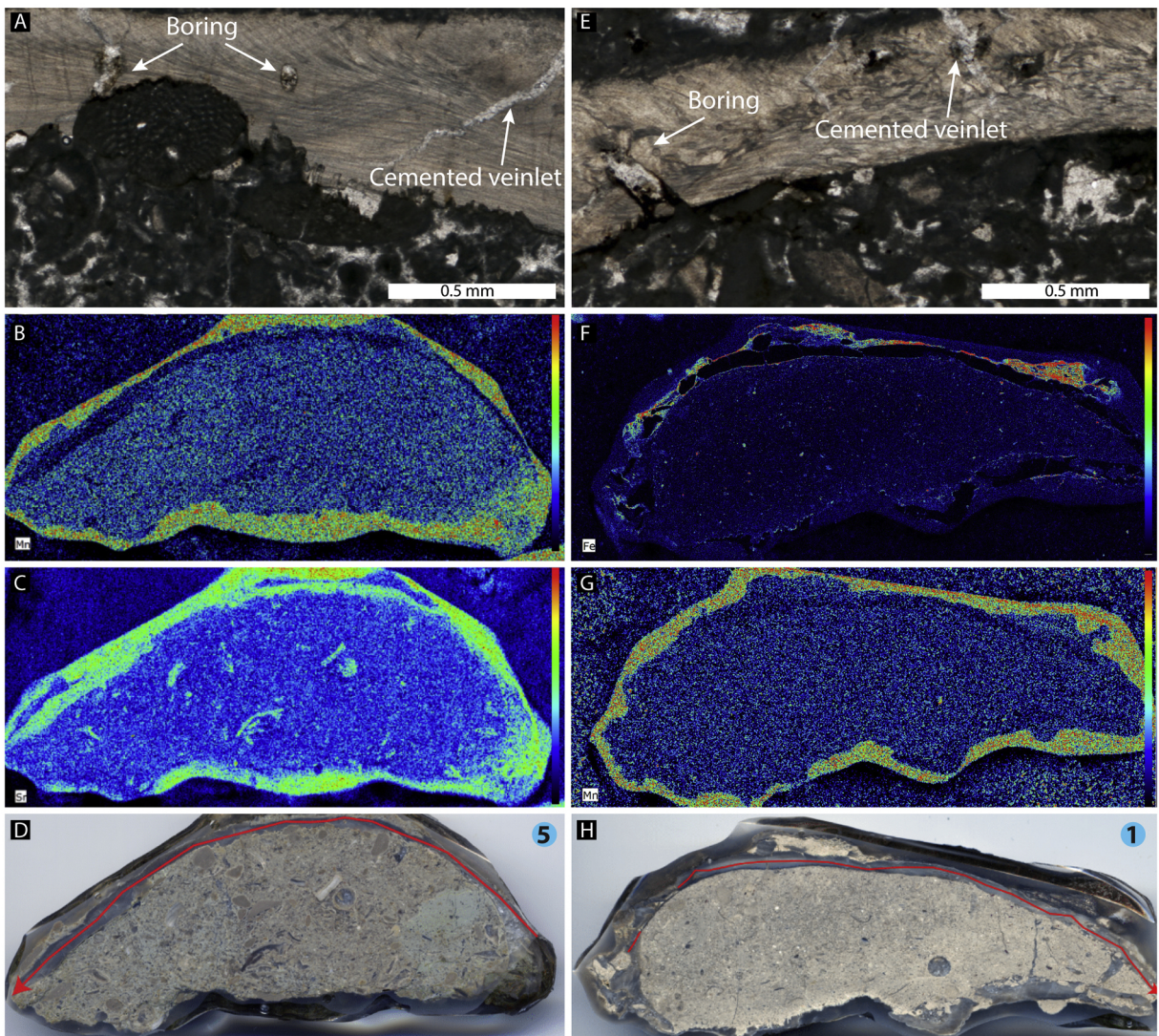


Figure 4

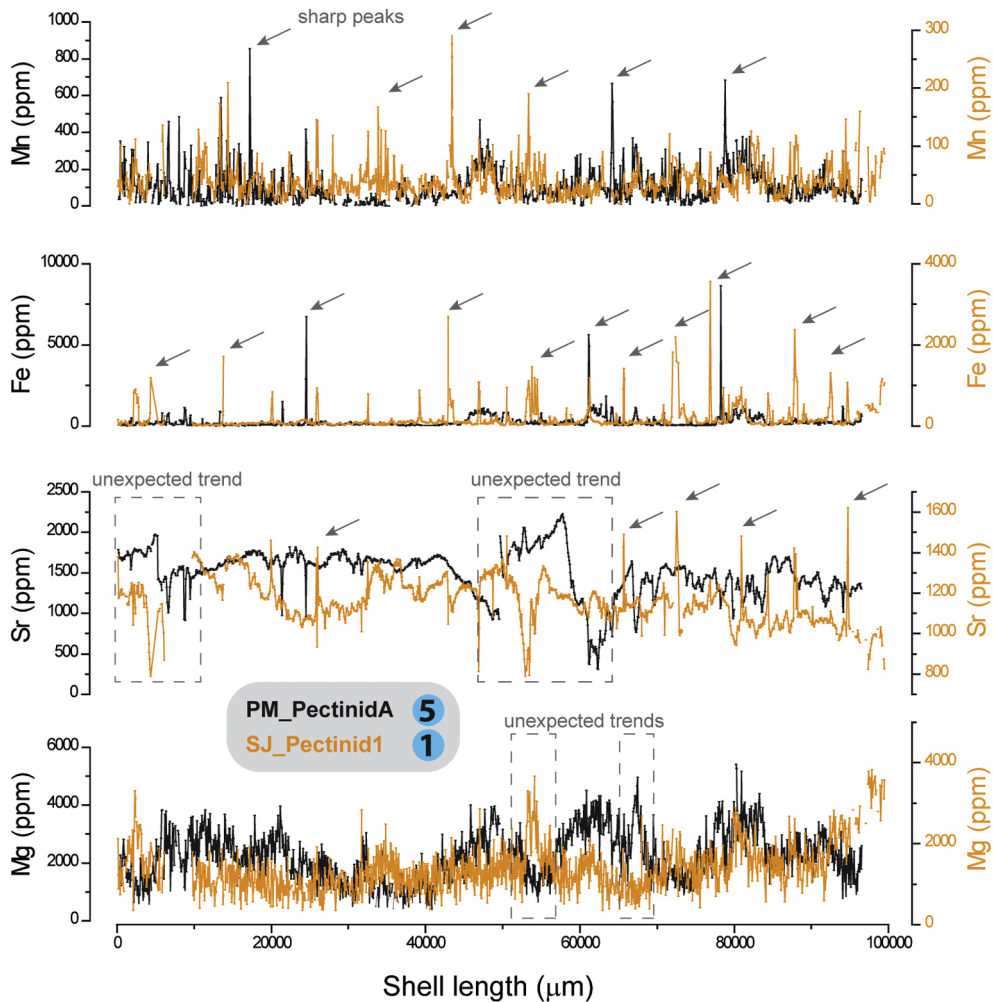


Figure 5

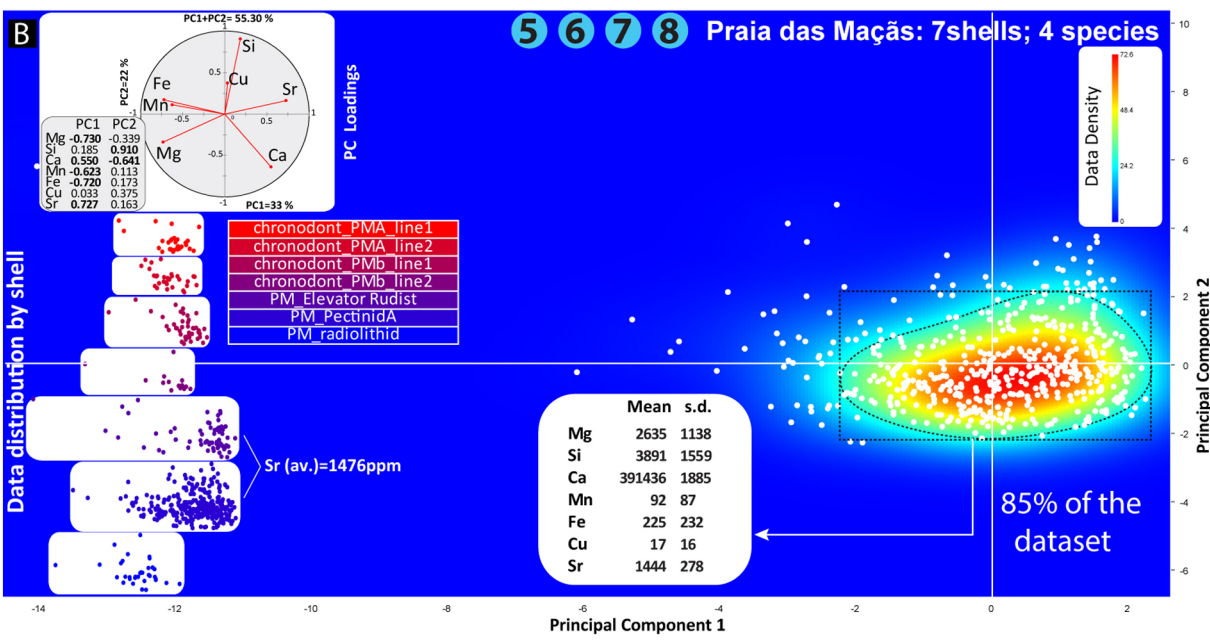
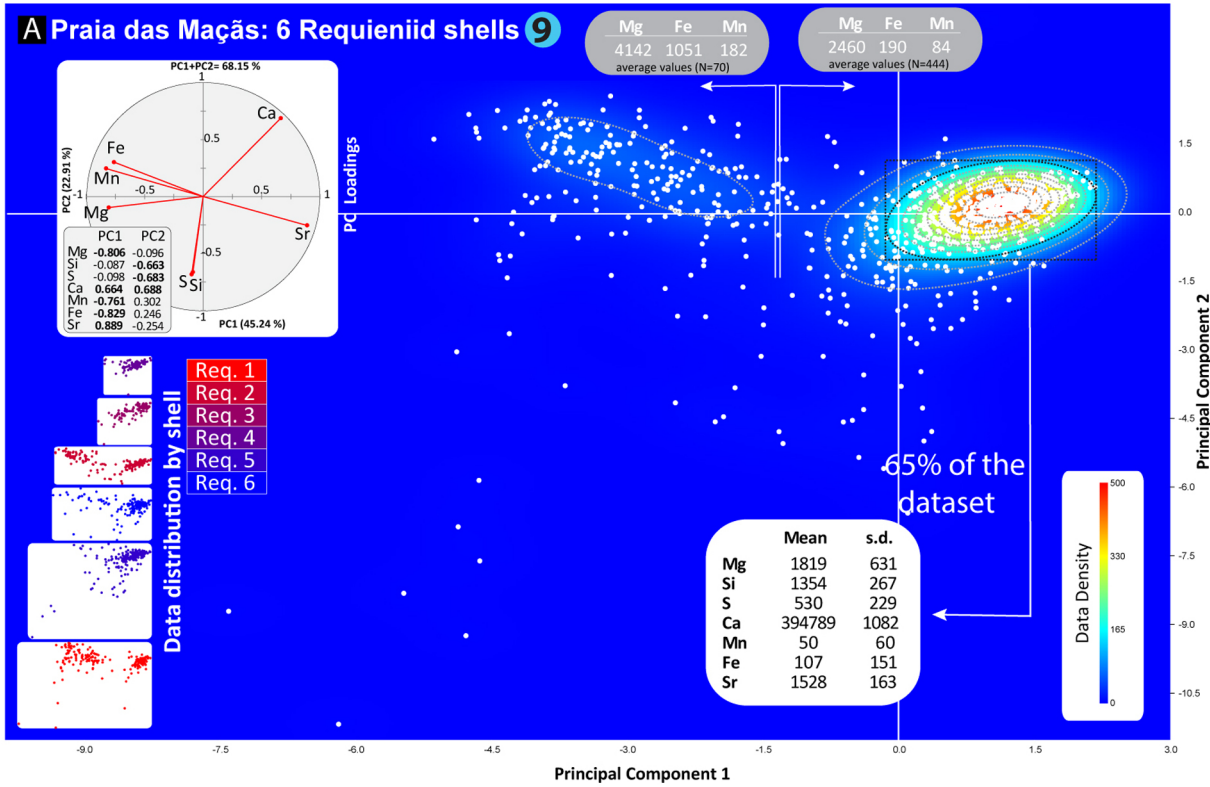


Figure 6



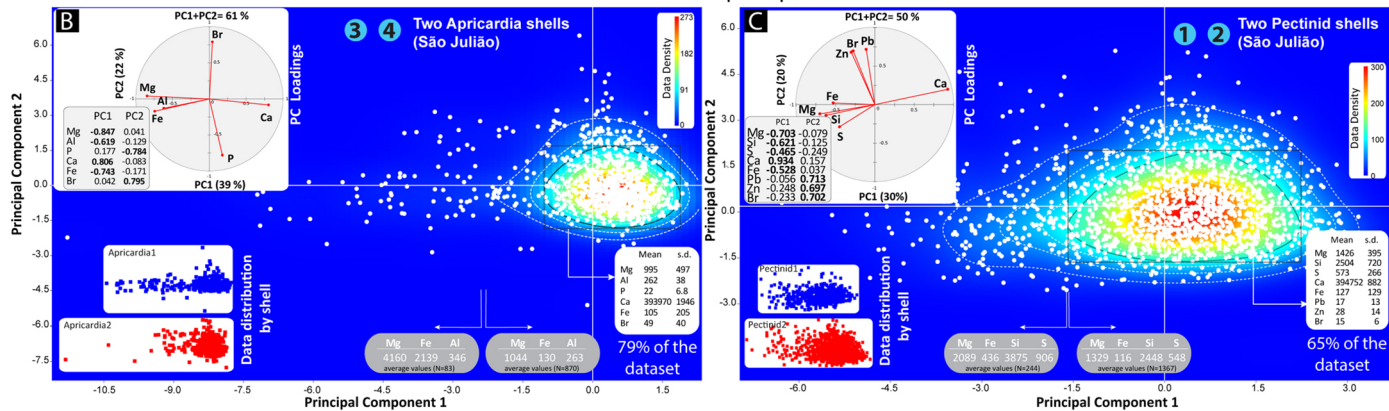
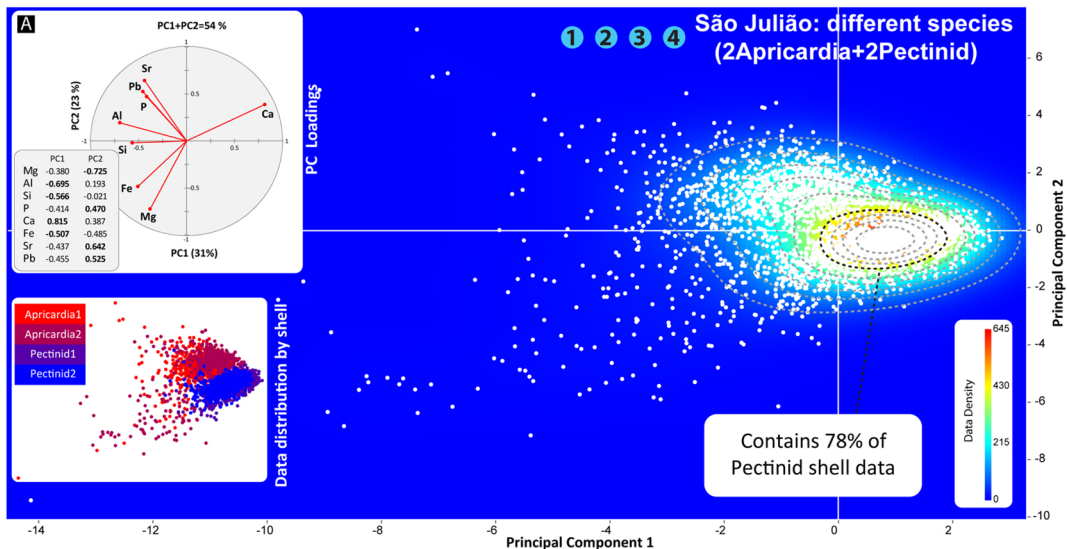


Figure 7

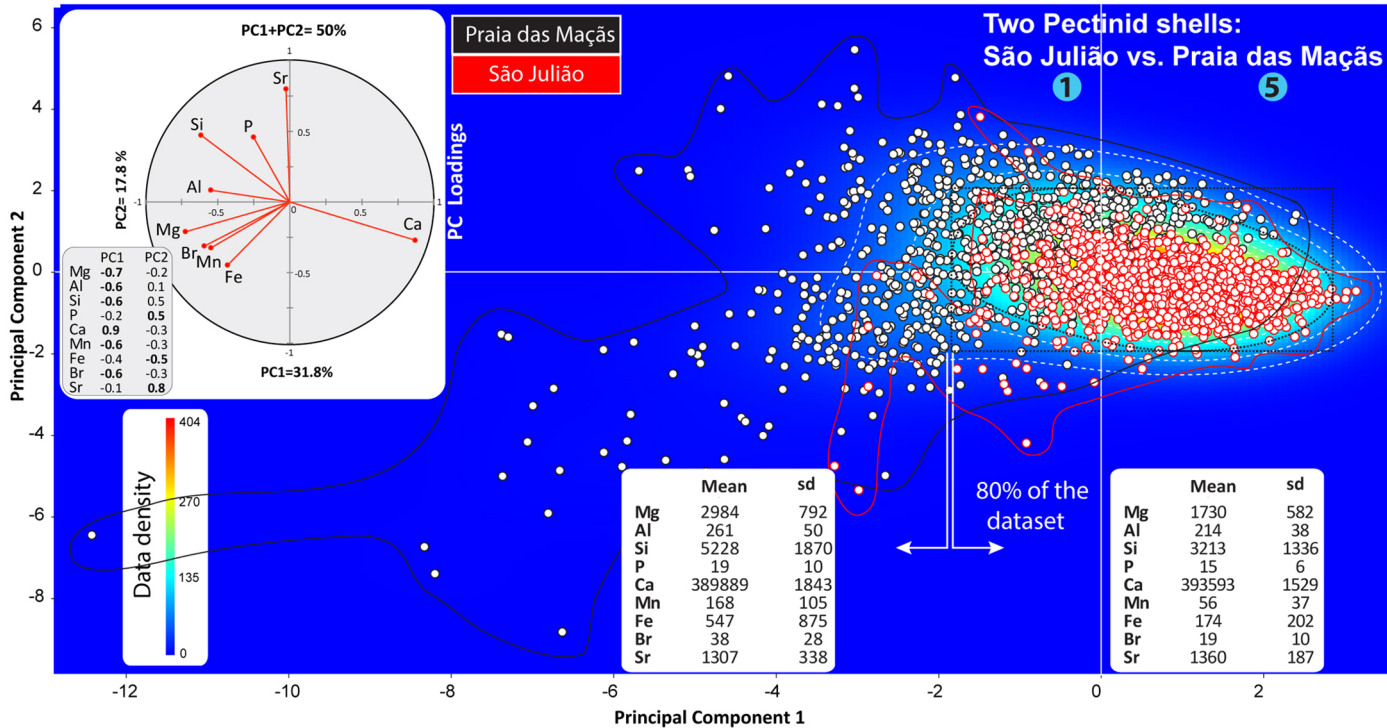


Figure 8

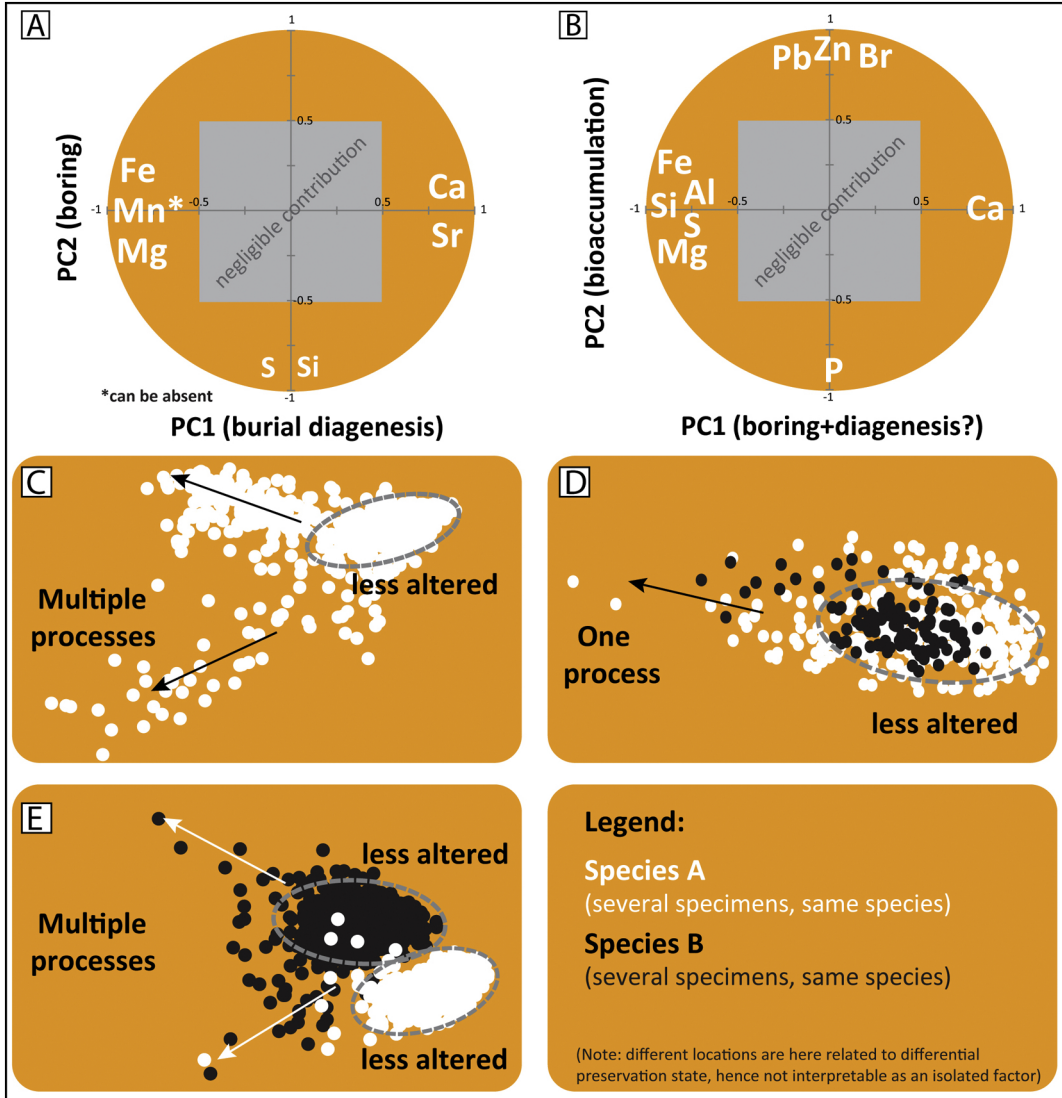


Figure 9



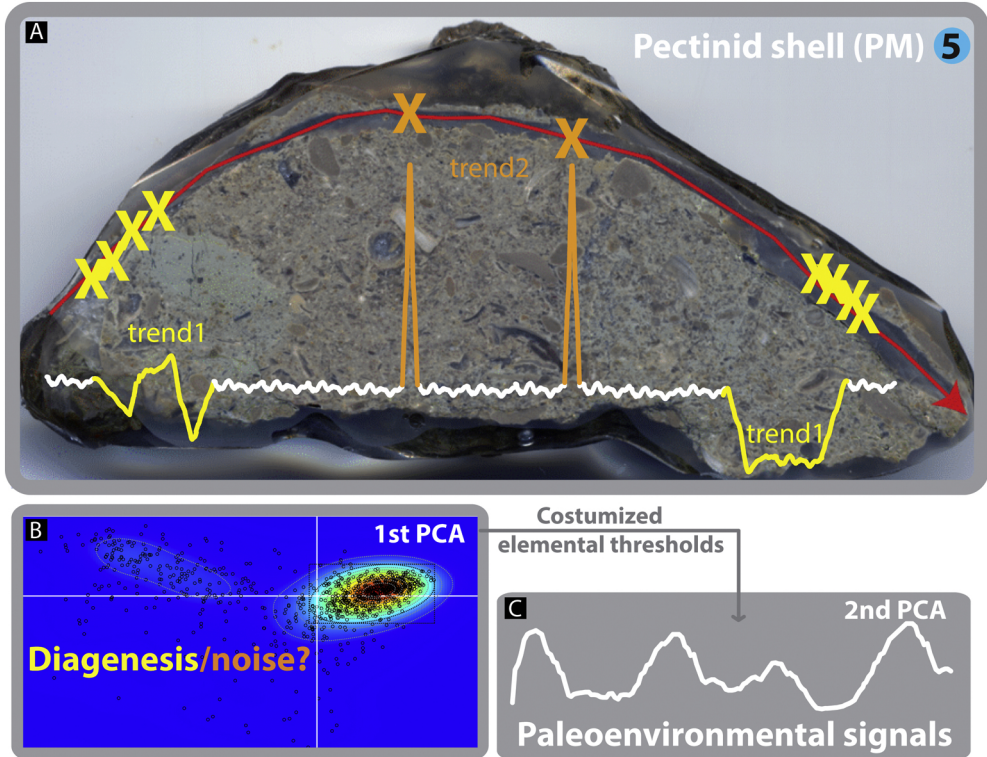


Figure 10

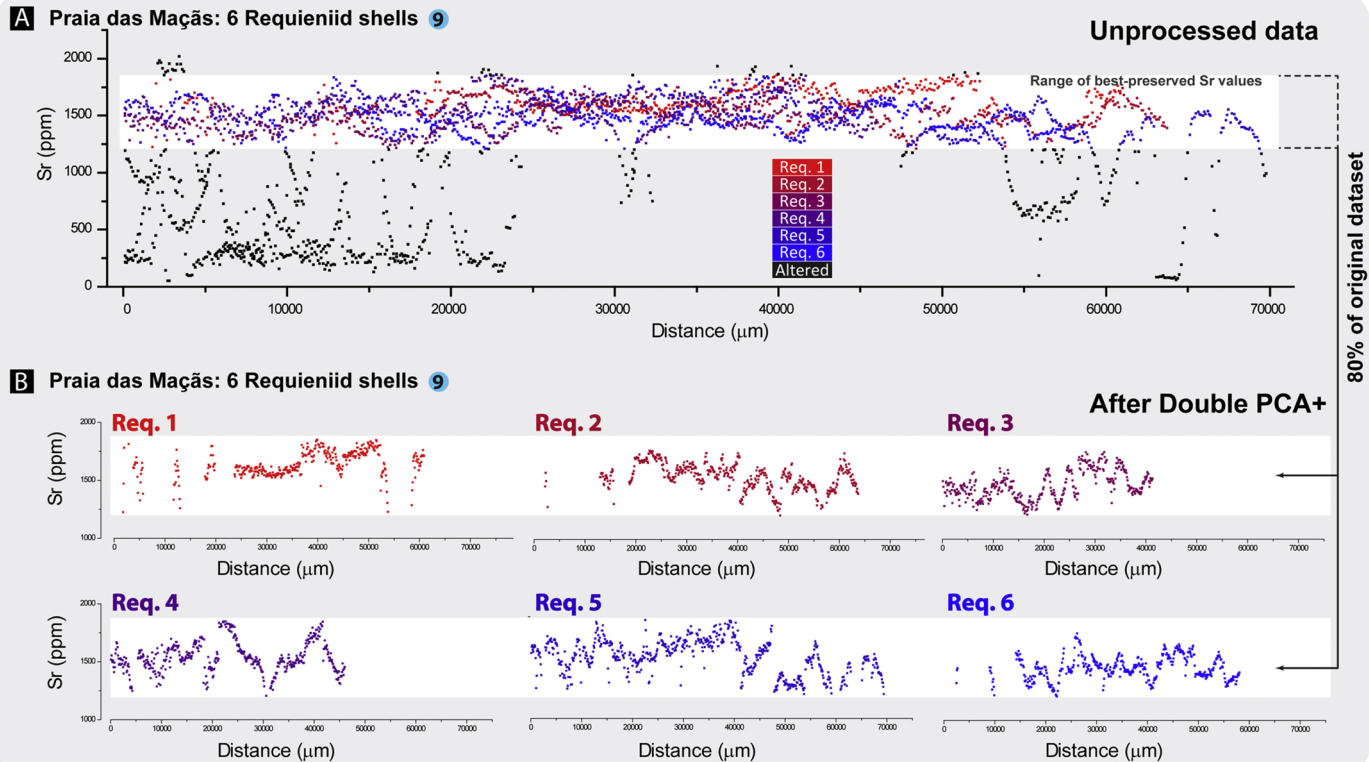


Figure 11

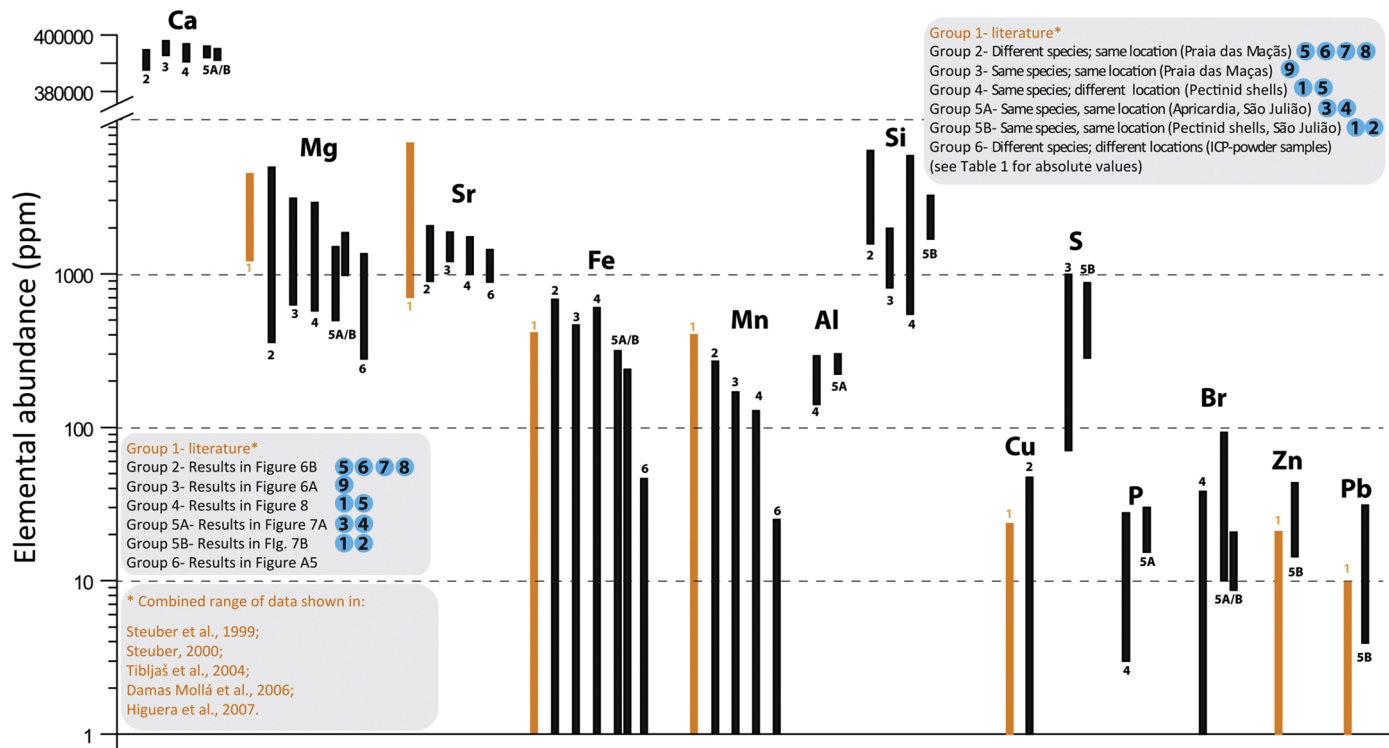


Figure 12